

Copyright  
by  
Rubin Sidhu  
2005

**The Dissertation Committee for Rubin Sidhu Certifies that this is the approved version of the following dissertation:**

**Indium Phosphide Based Photodiodes for Mid-wave Infrared Detection**

**Committee:**

---

Archie L. Holmes, Jr, Supervisor

---

Joe C. Campbell

---

Ananth Dodabalapur

---

Dean P. Neikirk

---

John G. Ekerdt

**Indium Phosphide Based Photodiodes for Mid-wave Infrared  
Detection**

**by**

**Rubin Sidhu, B. E.; M. S. E.**

**Dissertation**

Presented to the Faculty of the Graduate School of

The University of Texas at Austin

in Partial Fulfillment

of the Requirements

for the Degree of

**Doctor of Philosophy**

**The University of Texas at Austin**

**December 2005**

**Dedicated**

to

my parents

Harminder Singh Sidhu and Rajinderpal Kaur Sidhu

## **Acknowledgements**

Every successful Ph.D. project involves a mentor and a guide; someone who helps define the goals and understand the problems, who provides inspiration in difficult times, and who provides an environment conducive to research. Professor Archie Holmes has been that mentor and guide, and for that I am very grateful to him.

Professor Joe Campbell provided perspective that only someone with his experience and expertise could possess. I am thankful to him for welcoming my questions on a ‘walk-in’ basis, for sharing vital lab equipment, and for serving as the chairperson on my dissertation committee.

I am also grateful to Professor Ananth Dodabalapur, Professor Dean Neikirk, and Professor John Ekerdt for taking the time out of their busy schedules to serve on my dissertation committee. Their feedback on my research and this dissertation is appreciated.

This work would not have been possible without the help of my colleagues. I am deeply indebted to Xiaoguang Sun, Jeff Hurst, Mike Oye, Sridhar Govindaraju, David Gotthold, and Jason Reifsnider for all their help in the MBE lab. The MBE lab would not function without Terry Mattord, and I am thankful to him for fixing the mostly broken equipment. A sincere thank you goes to all the students in Dr. Campbell’s group who were always willing to help with device processing and measurements. I learned a lot from collaborations with

Geoff Kinsey, Shuling Wang, Gauri Karve, Xiaoguang Zheng, Xiaowei Li, Feng Ma, Ning Li, Ning Duan, Ning Tan, Zhengmao Ye, Mingguo Liu, Hao Chen and Lijuan Zhang.

Geoff Kinsey, Oleg Shchekin, and Dan Fine have been good friends at work and beyond. I am grateful to them for all their support and advice. Thanks also go to Oleg, Dan, and Richard Heller for donuts and coffee during the many long evenings spent in the lab.

The support and safety staff at the Microelectronics Research Center works tirelessly to keep the labs functional and safe. I am grateful to them for all their help and the lack of accidents. A big thank you goes to all the administrative staff, especially Amy Pinkston, for making sure that my paychecks always came on time, that my tuition was always paid, and that I never missed any deadlines.

I thank Raj Desikan for many delicious dinners. He has been the perfect roommate and a good friend.

Finally, a very special thank you goes to Jenny Mullins for her love and companionship.

# **Indium Phosphide Based Photodiodes for Mid-wave Infrared Detection**

Publication No. \_\_\_\_\_

Rubin Sidhu, Ph.D.

The University of Texas at Austin, 2005

Supervisor: Archie L. Holmes, Jr.

Mid-wave infrared (MWIR) photodetectors are used in many military and civil applications. Focal plane arrays made of these detectors are used for thermal imaging. In addition to high sensitivity, these devices require high degree of uniformity and operating temperatures close to room temperature. Current MWIR detectors are made from the mercury-cadmium-tellurium material system. These detectors suffer from poor uniformity and high fabrication costs associated with difficult device processing. MWIR detectors on Indium Phosphide substrates can take advantage of the mature materials and device technology of the Indium Phosphide material system. This material system has been used to make high performance devices for fiber optic communications for many years, and offers high uniformity and good yield. In this dissertation we present results from

Indium Phosphide based p-i-n and avalanche photodiodes with cutoff wavelength of  $2.4\mu\text{m}$ . These detectors utilized lattice matched GaInAs-GaAsSb type-II quantum wells for long wavelength absorption. The p-i-n devices had low dark current at low bias, and room temperature external quantum efficiency of 43% at  $2.23\mu\text{m}$ . The avalanche photodiodes were fabricated with an InP multiplication region and showed room temperature gain above 30. At 225K, these devices showed near breakdown dark current density of  $138\mu\text{A}/\text{cm}^2$  and gains above 200. Using strain-compensation in these type-II quantum wells, it may be possible to push the absorption of these photodiodes to longer wavelengths.



## Table of Contents

<b>LIST OF TABLES</b>	<b>XII</b>
<b>LIST OF FIGURES</b>	<b>XIII</b>
<b>CHAPTER 1 INTRODUCTION</b>	<b>1</b>
<b>CHAPTER 2 MID-WAVE INFRARED PHOTODETECTORS</b>	<b>4</b>
2.1 Introduction.....	4
2.2 Detector classification.....	5
2.3 Sensitivity and operating temperature.....	6
2.4 Material systems for MWIR detectors.....	6
2.4.1 HgCdTe photodetectors.....	8
2.4.2 GaAs based QWIPs and QDIPs.....	9
2.4.3 InAs and GaSb based photodetectors.....	10
2.4.4 InP based photodiodes.....	11
2.5 Type-II quantum wells.....	12
<b>CHAPTER 3 CRYSTAL GROWTH AND DEVICE PROCESSING</b>	<b>15</b>
3.1 Molecular Beam Epitaxy.....	15
3.2 Materials Characterization.....	18
3.2.1 Photoluminescence.....	19
3.2.2 X-ray Diffraction.....	19
3.3 MBE Growth of Mixed Group-V Materials.....	22
3.3.1 Sample Preparation.....	24
3.3.2 Effects of Growth Parameters on Antimony Incorporation.....	26

3.4 Device fabrication .....	31
3.5 Summary .....	32
<b>CHAPTER 4 PHOTODIODE CHARACTERIZATION</b>	<b>33</b>
4.1 Introduction .....	33
4.1 p-i-n and avalanche photodiodes .....	33
4.3 DC Characterization .....	34
4.4 Dark current .....	36
4.5 Spectral response .....	38
4.5.1 Responsivity and Quantum Efficiency .....	39
4.6 Noise .....	43
4.6.1 Detectivity .....	44
<b>CHAPTER 5 GAINAS-GAASSB <i>P-I-N</i> PHOTODIODES</b>	<b>46</b>
5.1 Introduction .....	46
5.2 The p-i-n Structure .....	46
5.3 MBE growth .....	47
5.4 Device Results .....	50
5.4.1 DC characteristics .....	50
5.4.2 Optical characterization .....	56
5.4.3 Responsivity .....	59
5.4.4 Dark-noise and detectivity .....	60

5.5 Summary .....	64
<b>CHAPTER 6 AVALANCHE PHOTODIODES WITH GAINAS-GAASSB TYPE-II QWS</b>	<b>66</b>
6.1 Introduction .....	66
6.2 The SACM Device Structure .....	67
6.3 Growth and Fabrication .....	69
6.4 Device Results .....	69
6.4.1 DC characteristics and avalanche gain .....	70
6.4.2 Optical response .....	73
6.4.3 Noise and detectivity .....	78
6.5 Summary .....	81
<b>CHAPTER 7 CONCLUSIONS AND FUTURE WORK</b>	<b>82</b>
7.1 Conclusions .....	82
7.2 Future work .....	83
<b>APPENDIX A</b>	<b>86</b>
<b>BIBLIOGRAPHY</b>	<b>90</b>
<b>PUBLICATIONS</b>	<b>95</b>
Journal Papers: .....	95
Conference Presentations: .....	96
<b>VITA</b>	<b>99</b>

## **List of Tables**

Table 1:	De-ox procedure used before p-i-n device growth.....	48
----------	--	----

## List of Figures

Figure 1. The electromagnetic spectrum .....	4
Figure 2. Detectivities of various infrared detectors .....	7
Figure 3. Bandgap vs. lattice-constant of III-V and II-VI materials. ....	8
Figure 4. Inter-band and intra-band transitions.....	10
Figure 5. Performance comparison of different InP based long-wavelength photodiodes .....	12
Figure 6. Band-lineup between $\text{Ga}_{0.47}\text{In}_{0.53}\text{As}$ and $\text{GaAs}_{0.51}\text{Sb}_{0.49}$ . The type-II transition is shown from the valence band of GaAsSb to the conduction band of GaInAs.....	13
Figure 7. Schematic diagram of the MBE reactor.....	16
Figure 8. X-ray diffraction setup.....	21
Figure 9. Measured (black) and simulated (red) x-ray rocking curves. ....	22
Figure 10. Schematic structure of an x-ray sample.....	24
Figure 11. RHEED patterns before (2x2) and after de-ox (2x4).. ....	25
Figure 12. X-ray diffraction data from samples grown at three different temperatures. ....	27
Figure 13. XRD data from samples grown at different group-III growth rates....	28
Figure 14. XRD data from samples grown with equal Arsenic and Antimony BEPs.....	29
Figure 15. Effect of Arsenic BEP on the composition of AlAsSb, for Antimony BEP = $3.0 \times 10^{-6}$ torr. ....	30
Figure 16. Principle of FTIR operation .....	39

Figure 17. Blackbody responsivity measurement apparatus. a: blackbody controller; b: Liquid nitrogen tube to the cryostat; c: Stanford Research Systems FFT spectrum analyzer; d: batteries used to bias the APD; e: Lakeshore temperature controller; f: Stanford Research Systems 570 current pre-amplifier; g: Cryostat with device mounted inside; h: blackbody source .....	42
Figure 18. Schematic diagram of the p-i-n device structure.....	47
Figure 19. Reverse I-V curves from a 64 microns diameter mesa device at different temperatures. ....	51
Figure 20. Room temperature dark current as a function of reverse-bias, for different diameter devices. ....	52
Figure 21. Room temperature dark-current vs. device diameter at two different reverse-bias voltages.....	52
Figure 22. Plot of log of the dark current vs. 1/T at two different reverse bias voltages .....	54
Figure 23. Room temperature shunt resistance (red circles) and $R_oA$ product (black triangles) from different diameter devices .....	56
Figure 24. Spectral response from the p-i-n device measured at -2V bias and at different temperatures. ....	58
Figure 25. Responsivity vs. wavelength at three different temperatures, measured at -2V bias.....	60
Figure 26. Dark noise vs. temperature measured at -2V bias from a 64 $\mu$ m diameter device.....	61

Figure 27. Specific detectivity at -2V as a function of wavelength measured at different temperatures. ....	62
Figure 28. Room temperature external quantum efficiency as a function of wavelength from devices with two different top surface coatings. The external quantum efficiencies were measured at -2V bias. ....	64
Figure 29. Schematic of the SACM avalanche photodiode structure and the electric- field distribution in the device at two different reverse bias voltages. ....	68
Figure 30. Reverse I-V data at different temperatures .....	70
Figure 31. Photocurrent (solid line), dark current (dashed lines) and avalanche gain (red circles) at room-temperature (top) and 225 K (bottom). ....	72
Figure 32. (a) The APD responsivity measurement apparatus and (b) the equivalent biasing circuit using 9V batteries. a: 9V batteries in series with the photodiode and the pre-amplifier input; b: temperature controller; c: SRS 570 pre-amplifier; d: cryostat with the device inside; e: blackbody source. ....	74
Figure 33. Photo-response of the APD at different temperatures, measured at -37V bias. ....	75
Figure 34. Room-temperature spectral response of the APD at different reverse-bias voltages. ....	76
Figure 35. Room-temperature responsivity vs. wavelength of the APD at -37V bias. The equivalent external quantum efficiency is represented by the grey (dashed) lines and numbers in red .....	77

Figure 36. Noise-current from the APD vs. reverse bias voltage, measured at 225K (black circles) and room-temperature (red triangles).....	78
Figure 37. APD noise-current vs. temperature, measured at punchthrough (- 37V).....	79
Figure 38. Detectivity vs. wavelength at different reverse bias voltages, measured at 225K (top) and room temperature (bottom). ....	80



## Chapter 1 Introduction

Photodetectors sensitive to the mid-wave infrared (MWIR) wavelengths ( $2\mu\text{m} - 5\mu\text{m}$ ) are used in various applications such as chemical sensing, gas monitoring, medical diagnostics, high speed IR-imaging, and free-space communications [1-4]. Many important molecules have absorption lines in this wavelength range, including  $\text{NO}_2$ ,  $\text{NH}_3$ ,  $\text{C}_2\text{H}_2$ ,  $\text{HF}$  etc. Some important atmospheric pollutants like  $\text{CO}$ ,  $\text{N}_2\text{O}$  and  $\text{CH}_4$  also have some absorption in the  $2\mu\text{m}$ - $3\mu\text{m}$  wavelength range. This absorption, mostly by the overtones and combination rotational-vibrational bands, is 2 to 3 orders of magnitude weaker than their fundamental band absorptions which are at much longer wavelengths. The weak absorption coefficients in the MWIR region allow long range and remote sensing of these species. The high atmospheric transmission in this window also makes these wavelengths attractive for ground-based astronomical observations and imaging [5]. One example of the medical diagnostic applications of MWIR detectors is non-invasive blood glucose determination [6, 7]. Focal plane arrays are fabricated from these detectors for many thermal imaging and tracking applications [8-12].

The requirements of a good photodetector for MWIR applications include high sensitivity; low dark current; low noise; high speed; and a high operating temperature, ideally at/near room temperature. The predominant technologies for MWIR detection use the Mercury-Cadmium-Tellurium (MCT) material system [13]. MCT detectors for  $2\mu\text{m}$ - $3\mu\text{m}$  detection operate within the TE cooler range

[13]. This material system, however, suffers from poor uniformity, which leads to low yield and high costs [14]. Lack of uniformity also severely undermines the focal plane array performance. These shortcomings in the MCT system have led to research efforts investigating alternative technologies for MWIR detection, such as InAs/GaInSb detectors, quantum well infrared photodetectors (QWIPs) and quantum dot infrared photodetectors (QDIPs.) Detectors using these alternative technologies require significantly lower temperatures ( $<150\text{K}$ ) for operation [11, 15, 16]. At higher temperatures, these devices suffer from high dark current, and the noise associated with it leads to low detectivity values. The dark current at low bias and low temperature is limited by thermal generation, and at high bias, is limited by tunneling. Operation at low temperatures requires bulky and expensive cooling equipment which adds to the system complexity and cost.

Detectors using GaInAs/GaAsSb type-II QWs on InP are promising candidates for detection in the MWIR region, especially at operating temperatures close to ambient. These devices can benefit from the mature InP materials and device technologies. The high electron effective mass (compared to the MCT material system) also allows higher density of states and low tunneling current [17]. In this dissertation, I present results from p-i-n and avalanche photodiodes that we fabricated on InP using GaInAs-GaAsSb type-II quantum wells for long-wavelength absorption. The p-i-n devices exhibited low dark-current and 43% room-temperature external quantum efficiency at  $2.24\mu\text{m}$ . The avalanche photodiodes showed room-temperature gains up to 35 and 225K gains up to 250 with spectral response similar to the p-i-n devices.

This dissertation is organized as follows: Chapter 2 in this dissertation discusses some of the alternative technologies being investigated from MWIR detection. The band line-ups of GaInAs-GaAsSb alloys and the principle of operation of our InP based MWIR detectors using type-II quantum wells is also explained in this chapter. A brief explanation of the various figures of merit used to report photodiode performance is provided in Chapter 3, along with a description of some of the measurement and test setups used in this work.

Chapter 4 explains the MBE growth of GaAsSb. The effects of growth parameters on the crystal quality and composition are reported. A brief description of the device fabrication is also provided in this chapter.

Chapter 5 and Chapter 6 describe the p-i-n and avalanche photodiodes respectively. A detailed description of the device structures is provided. The results of DC and optical characterization are reported, and various performance related issues are discussed. Finally, Chapter 7 includes some concluding remarks and future work that can be carried out to improve the performance of InP based MWIR detectors.

## Chapter 2 Mid-wave Infrared Photodetectors

### 2.1 INTRODUCTION

Infrared radiation is a part of the continuous electromagnetic spectrum, illustrated in Figure 1. The boundaries between the various sections such as UV, visible, infrared, etc. are loosely defined. The infrared wavelengths extend from about  $1\mu\text{m}$  to about  $1000\mu\text{m}$ . The mid-wave infrared (MWIR) spectrum spans the  $2\mu\text{m}$  to  $5\mu\text{m}$  region. MWIR detectors are used in many important applications, as discussed in Chapter 1. Several different material systems and technologies are used to make MWIR detectors, some of which are discussed in this chapter.

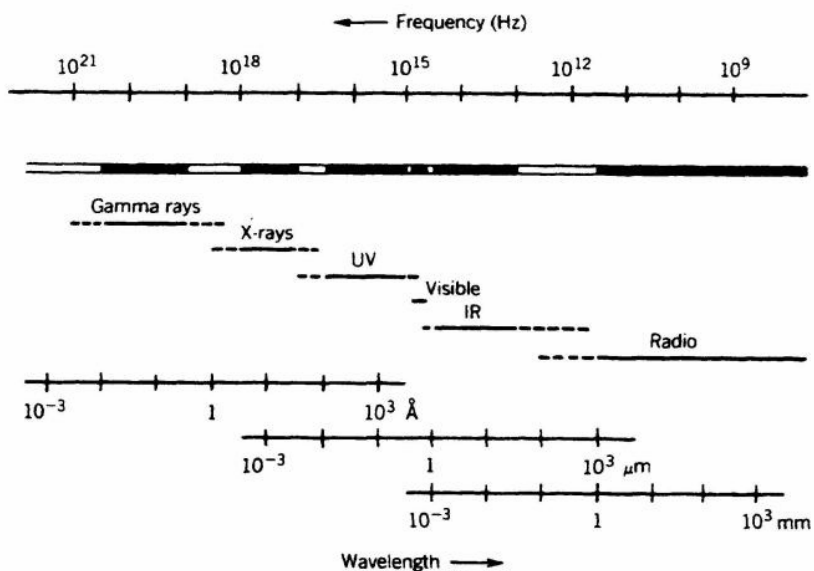


Figure 1. The electromagnetic spectrum [18].

## **2.2 DETECTOR CLASSIFICATION**

Infrared detectors are broadly classified into thermal detectors and photon (quantum) detectors. Thermal detectors measure one of the secondary effects associated with the absorption of infrared radiation, such as increase in temperature. These detectors can operate at room temperature but are slow and comparatively less sensitive. The principle of photon or quantum detector operation involves the change in electrical properties in a material associated with the absorption of photons. In these detectors, electrons absorb a photon of incident radiation and jump to a higher energy state. Photon detectors are further classified into photoconductive (PC) and photovoltaic (PV) detectors.

Photoconductive detectors are made of a material with poor conductivity. This conductivity increases with incident radiation intensity, because of photo-generated carriers. The increased conductivity leads to an increased current if a voltage is applied across the detector. PC detectors are passive devices and no potential difference is created across the terminals of these devices because of absorbed radiation.

Photovoltaic detectors on the other hand are diodes which produce a voltage across the terminals when photons are absorbed. This potential difference can cause current flow. In some cases, these diodes may be reverse biased to produce a high electric field in the depletion region around the p-n junction. Any photo-generated carriers in this region drift to the appropriate electrodes, thereby causing an increased reverse current in the diode which scales with the intensity

of the incident radiation. PV detectors generally have a higher signal-to-noise ratio (SNR) than PC detectors.

### **2.3 SENSITIVITY AND OPERATING TEMPERATURE**

Primary detector requirements for most applications include high sensitivity, high speed, and high operating temperature. The sensitivity of a detector scales inversely with the noise. Noise is any current (or voltage) that is not caused by the incident signal of interest. Many different mechanisms contribute to noise, and are discussed in Chapter 4. Majority of the noise in infrared detectors is caused by mechanisms triggered by the transfer of thermal energy from the lattice to the electrons. To minimize the noise from such mechanisms, the detectors are operated at low temperatures. In general, detectors with smaller absorption bandgaps require lower operating temperatures. These cooling systems add to the system complexity and cost. Detectors that require operating temperatures below 200K are difficult to incorporate into small portable systems, as required for many applications.

### **2.4 MATERIAL SYSTEMS FOR MWIR DETECTORS**

Semiconductor materials, including the group-IV, III-V compounds, and the II-VI compounds, are used to make different types of photodetectors in all of the above mentioned categories. Figure 2 shows the typical absorption wavelengths and detectivity values for many detector technologies, along with their operating temperatures. A brief description of the primary material systems

and detector technologies used for MWIR detection is presented in the subsequent sections of this chapter. Detailed information on infrared detector technology can be found in [18]. An overview of the state-of-the-art in infrared detectors can be found in [19, 20].

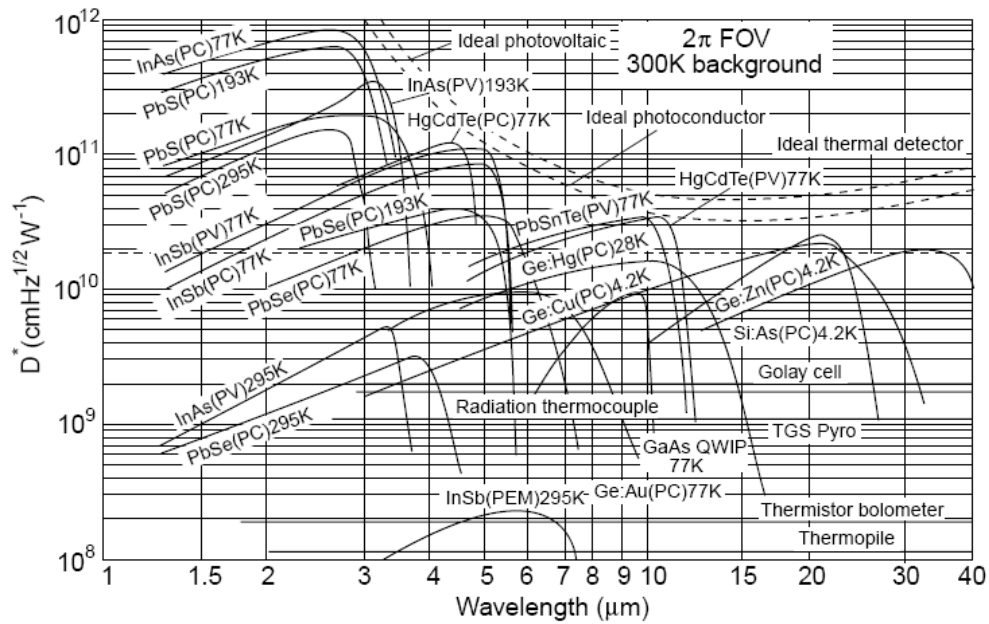


Figure 2. Detectivities of various infrared detectors [20].

The primary material systems used to fabricate MWIR photon detectors include HgCdTe, GaAs/AlGaAs, GaAs/GaInAs, InAs/GaInSb, and InP/GaInAs. Figure 3 shows the bandgap vs. lattice constant diagram for the III-V and the II-VII material systems.

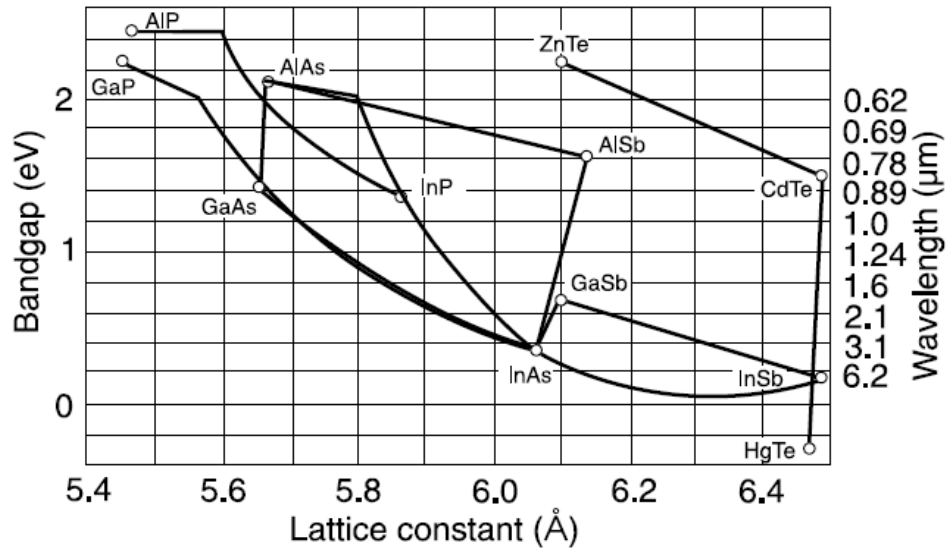


Figure 3. Bandgap vs. lattice-constant of III-V and II-VI materials [21].

### 2.4.1 HgCdTe photodetectors

HgCdTe alloys are used to make both PC and PV detectors. The bandgap of  $(\text{HgTe})_x(\text{CdTe})_{1-x}$  alloys can be tailored from  $0.7\mu\text{m}$  to  $25\mu\text{m}$  [21]. These devices are grown lattice-matched to CdZnTe substrates using liquid phase epitaxy (LPE), molecular beam epitaxy (MBE) and metal-organic chemical vapor deposition (MOCVD). Photodiodes or photodiode-arrays are generally fabricated for short-wave and mid-wave IR detection. Some initial work on near-IR avalanche photodiodes has been reported in [22]. MWIR HgCdTe photodiodes are the best performing devices in the thermoelectric (TE) cooler range [13]. Typical  $R_0A$  products of  $10^5 \Omega\text{cm}^2$  below 200K are reported for HgCdTe detectors with cutoff wavelengths of about  $5\mu\text{m}$  [8, 11, 21].



HgCdTe detectors suffer from poor material uniformity because of high etch-pit density on epitaxially grown layers. The weak Hg-Te bond limits the temperature at which these materials can be processed into devices. For the same reason, it is very difficult to passivate the mesa walls of these detectors. Poor passivation results in high leakage currents and reduced detectivity.

#### **2.4.2 GaAs based QWIPs and QDIPs**

Quantum well infrared photodetectors (QWIPs) and quantum dot infrared photodetectors (QDIPs) use the bound to bound state or bound to continuous state electron transitions. Figure 4 compares the inter-band and intra-band transitions. QWIPs and QDIPs are usually fabricated as photoconductors on GaAs substrates to take advantage of the well developed material system. Some InP based devices have also been reported [23]. On GaAs substrates, AlGaAs quantum wells are used for QWIPs, while GaInAs quantum dots are used in QDIPs. A detailed description of the QWIP technology is available in [24]. A comparison between HgCdTe and QWIP photodetector performance is presented in [11]. An overview of QDIP technology can be found in [15, 25]. QWIPs and QDIPs are generally designed for operation in the long wavelength window (8 $\mu$ m-12 $\mu$ m). Their operation is limited to temperatures below 77K. At higher temperatures, these devices have seriously degraded performance because of high leakage currents.

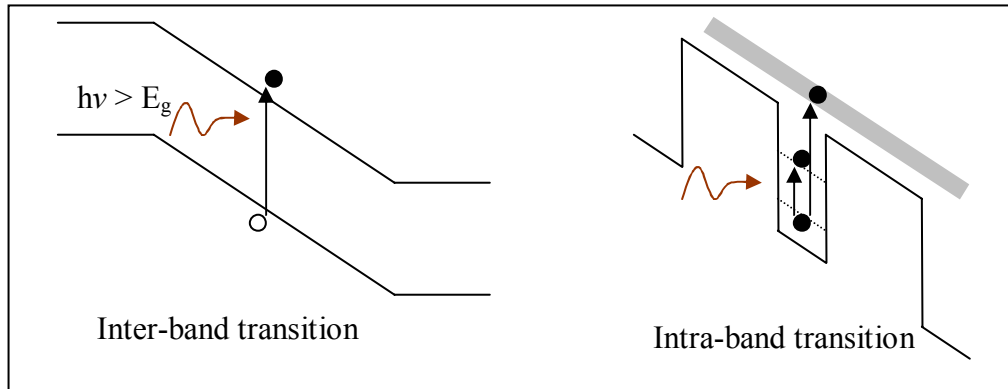


Figure 4. Inter-band and intra-band transitions.

### 2.4.3 InAs and GaSb based photodetectors

Mid-wave and long-wave IR photoconductors and photodiodes are fabricated on InAs and GaSb substrates using the lattice-matched and moderately strained layers. InAs has a bandgap of about 0.35eV at room temperature [26], corresponding to a wavelength of 3.5 $\mu\text{m}$ . InAs photodiodes have typical  $R_0A$  products of about  $10^6 \Omega\text{cm}^2$  for zero bias operation at 77K, and about  $10^4 \Omega\text{cm}^2$  at 120K. The performance degrades significantly at higher temperatures [19].

The InAsSb alloys can be grown compressively strained on InAs substrates, or lattice-matched to GaSb substrates. The latter span the 1.7 $\mu\text{m}$  to 4.2 $\mu\text{m}$  spectral range with  $R_0A$  products of about  $10^9 \Omega\text{cm}^2$  at 77K.

GaInSb and InAs have a staggered band-offset and form type-II structures (explained in the next section). These photodiodes with InAs-GaInSb strained-layer superlattices (SLS) have cutoff wavelengths up to 10 $\mu\text{m}$  [16, 17, 27]. High performance operation is still limited to temperatures well below 200K [20].

#### **2.4.4 InP based photodiodes**

The InP based materials have long been used to make high performance photonic devices in the 1.1 $\mu\text{m}$  - 1.6 $\mu\text{m}$  wavelength range. The mature device technology results in high yield and good uniformity across 4" substrates. The smallest bandgap material lattice-matched to the InP substrate is Ga<sub>0.47</sub>In<sub>0.53</sub>As, with a bandgap of about 0.75eV (1.65 $\mu\text{m}$ ) at room temperature. Photodiodes with response up to about 2 $\mu\text{m}$  have been demonstrated using GaInAs-GaInP strain compensated quantum wells [28, 29]. Longer wavelength absorption, up to about 2.6 $\mu\text{m}$ , is possible by using mismatched GaInAs on relaxed InAsP buffer layers on InP [30-32]. These devices suffer from residual defects propagating from the relaxed buffer layers into the photodiode active regions. These defects cause increased dark current and reduced detectivity. Figure 5 shows the comparative room temperature performance of various InP based photodiodes.

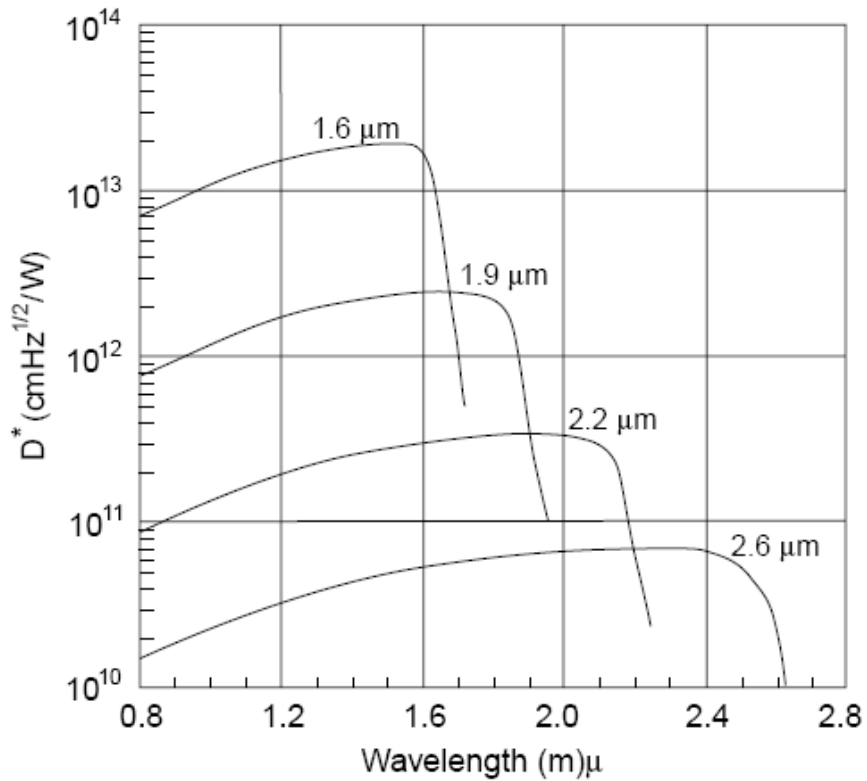


Figure 5. Performance comparison of different InP based long-wavelength photodiodes [20].

## 2.5 TYPE-II QUANTUM WELLS

A study of the band-offsets of  $\text{Ga}_{0.47}\text{In}_{0.53}\text{As}$  and  $\text{GaAs}_{0.51}\text{Sb}_{0.49}$  (both compositions lattice-matched to InP) shows that these materials have a type-II band lineup [26]. If multiple thin layers of these materials are grown adjacent to each other, type-II quantum wells can be formed. In these quantum wells, the electrons and holes are confined in adjacent layers. A spatially-indirect transition becomes possible across the layer interfaces. This transition has an effective

bandgap smaller than the regular bandgap of either of the two layers. Thus longer wavelengths of light can be absorbed. Figure 6 shows a schematic of the type-II quantum wells on InP.

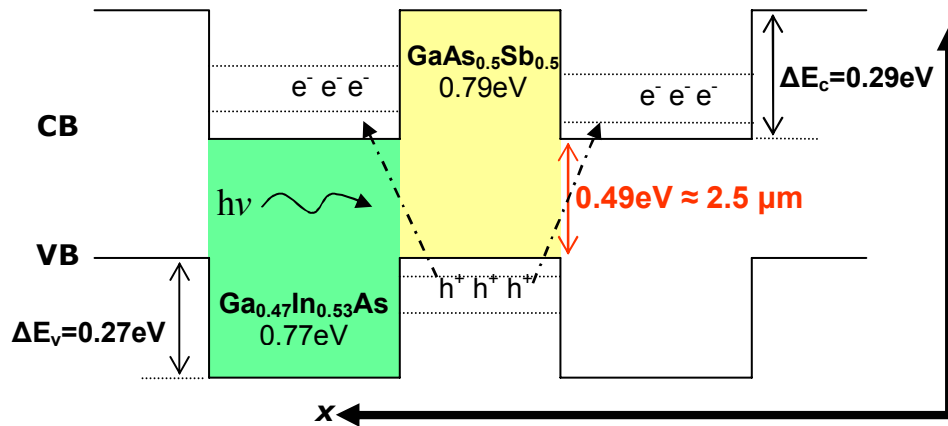


Figure 6. Band-lineup between  $\text{Ga}_{0.47}\text{In}_{0.53}\text{As}$  and  $\text{GaAs}_{0.51}\text{Sb}_{0.49}$ . The type-II transition is shown from the valence band of  $\text{GaAsSb}$  to the conduction band of  $\text{GaInAs}$ .

The type-II transition is tunneling assisted. The electron and hole wavefunctions penetrate into the barriers to some extent and result in a finite overlap between the wavefunctions. Photoluminescence data from such transitions is reported in [33, 34]. Light emitting diodes (LEDs) and lasers diodes employing type-II quantum wells have been reported in [35]. Accurate tuning of the operational wavelength is possible by varying the layer compositions and thicknesses.

We have fabricated p-i-n photodiodes and avalanche photodiodes on InP substrates using these lattice-matched type-II quantum wells. The crystal growth

and device fabrication methods, and device results are presented in the following chapters.

## Chapter 3 Crystal Growth and Device Processing

### 3.1 MOLECULAR BEAM EPITAXY

Molecular beam epitaxy (MBE) was developed by Al Cho and J. R. Arthur at AT&T Bell labs in the early 1970s [36, 37]. Since then, it has developed into a sophisticated tool for crystal growth for high performance electronic and optoelectronic devices. Today, MBE is perhaps the most versatile technique available to deposit high purity thin films of metals, semiconductors and insulators with very precise layer and composition control.

A typical MBE reactor is an ultra-high vacuum chamber wherein high purity source materials are thermally evaporated. The evaporated atoms or molecules have a long mean-free path because of low pressure ( $\sim 1 \times 10^{-9}$  torr.) inside the chamber. The molecular (or atomic) beams of these evaporated species are directed onto a heated substrate for film deposition. Precise control of the source material flux, substrate temperature, and other growth parameters is possible through the use of in-situ and ex-situ measurement and control systems. A detailed description of MBE equipment and technology is available in [38, 39].

All the material and devices for the research presented in this dissertation were grown in a modified Varian Gen-II reactor housed in the Microelectronics Research Center at The University of Texas at Austin. Figure 7 shows a schematic diagram of the MBE reactor.

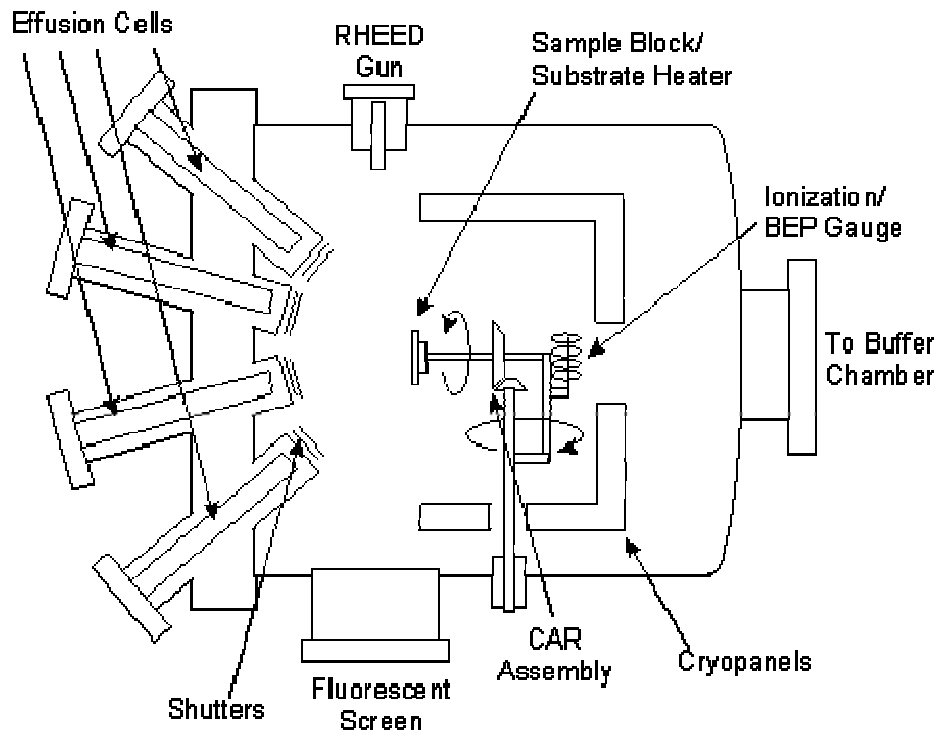


Figure 7. Schematic diagram of the MBE reactor. Adapted from [40]

The reactor has effusion cells for the group-III metals (Aluminum, Gallium, and Indium). The flux from these cells can be accurately controlled by controlling their temperature, which is measured by a thermocouple and controlled by a PID temperature controller. Pneumatically-actuated mechanical shutters are placed in front of the cells to turn the flux on and off. A Veeco dual-dopant effusion cell provides Silicon and Beryllium for n-type and p-type doping respectively. The reactor has also been fitted with three valved-cracker sources for Arsenic, Phosphorus, and Antimony. The Arsenic and Antimony valved-crackers use a two stage construction. The first stage is a sublimator where the loaded charge is evaporated as  $\text{As}_4$  or  $\text{Sb}_4$ . These species then pass through a very hot



tube (typically maintained between 800°C and 1000°C) where they crack to monomers and dimers. The Phosphorus cracker is a three stage source and takes red phosphorus as the charge. This can be sublimated between 300°C and 400°C and re-condensed in a separate zone at about 40°C as white Phosphorus. During operation, the red zone is maintained at 200°C to insure that there is no evaporation of red Phosphorus. The white zone is heated to about 70°C and it provides a very stable flux composed mainly of P<sub>4</sub>. This flux passes through a hot cracking tube where it dissociates mainly into P and P<sub>2</sub>.

A group-V flux composed mainly of monomers is generally desirable for high incorporation ratio and good crystal quality [41]. However, even at high cracking temperatures, the cracking efficiency (defined as the ratio of number of monomers to the sum of all species) is about 90%. Mechanical valves in the cracker tubes provide accurate and reproducible control over the group-V flux.

The substrate is mounted on a Molybdenum block, which is then secured onto the Continual Azimuthal Rotation (CAR) assembly. The CAR assembly rotates and heats the substrate during growth. Substrate rotation helps growth uniformity from substrate center to the edges. Substrate temperature is monitored using two independent systems: a thermocouple fitted behind the Molybdenum block, and an external infrared pyrometer. An ionization gauge is also fitted on the CAR. The CAR can be rotated such that the ionization gauge can be placed at the substrate growth position. In this position, the ionization gauge can read the beam equivalent pressure (BEP) of the incident flux. This is one of the ways to calibrate the source flux, but is used mainly to determine and set the group-V flux.

Metals (group-III materials) tend to coat the ionization gauge; therefore the flux readings are not accurate. Group-III flux is determined using the oscillations in intensity of the Reflection High Energy Electron Diffraction (RHEED) spot [39]. The surface condition of the substrate can also be monitored using RHEED technique where an electron beam is incident on the substrate at a glancing angle ( $1^\circ - 4^\circ$ ). The diffracted beam is collected on a fluorescent screen. Additionally, the RHEED technique is also used for verification of thermal desorption of the native oxides from the substrate surface, and surface temperature determination. The native oxides formed on certain substrates thermally desorb at a fixed temperature. Associated with this desorption is a change in the RHEED pattern. This change in pattern can be correlated to the substrate temperature and serves as an independent method of temperature calibration. The oxides on the GaAs substrate, for example, desorb at  $580^\circ\text{C}$  under Arsenic flux.

Two CTI Cryogenics cryo-pumps are used to pump the chamber down to background pressure of the about  $10^{-10}$  torr. A quadropole mass-spectrum analyzer is also installed on the MBE system to determine the various species present in the chamber.

### **3.2 MATERIALS CHARACTERIZATION**

A host of characterization tools can be used to study the material composition and crystal quality, e.g. photoluminescence (PL), x-ray diffraction, (XRD), atomic force microscopy (AFM), scanning electron microscopy (SEM),

tunneling electron microscopy (TEM), Hall measurements, etc. All materials characterization reported in this dissertation was done using PL and XRD.

### **3.2.1 Photoluminescence**

Photoluminescence (PL) is a powerful tool to determine the optical properties of materials. In this technique, the material under investigation is optically pumped using a laser spot with high power density. If the incident laser light is shorter in wavelength than the bandgap of the material of interest, the light is absorbed and electron hole pairs are created in the layer. Some fraction of these electron-hole pairs radiatively recombine to emit the PL signal. The energy of the emitted light is the energy difference between the electron and hole levels in the active layer; thus the emission wavelength points to the material's energy bandgap. This emitted light as a function of wavelength is measured using a spectrometer. Intensity and wavelength information from PL can be correlated with the material composition, material quality, defect states and their energy distributions. PL experiments can be carried out at various temperatures and under different incident illumination intensities for detailed analysis of defect states. In the work presented here, photoluminescence was used to optimize the crystal quality of GaInAs and GaAsSb layers on InP.

### **3.2.2 X-ray Diffraction**

X-ray diffraction (XRD) is another versatile non-destructive tool used for materials characterization. In this technique, the incident x-ray beam is reflected from parallel crystal planes in the sample. Bragg's diffraction condition occurs

when the path difference between successive reflections is an integral multiple of the x-ray wavelength. The condition is defined by:

$$n\lambda = 2d \sin \theta \quad \dots(3.1)$$

where 'n' is the diffraction order, ' $\lambda$ ' is the wavelength of the x-rays, 'd' is the spacing between successive reflecting planes, and ' $\theta$ ' is the angle of incidence. At this condition, constructive interference in the reflected beam leads to an intensity peak. Figure 8 shows the schematic setup for x-ray diffraction rocking curve measurements.

Detailed information on x-ray diffraction is available in [42]. A sample rocking curve from a symmetric (004)  $\omega$ -2 $\theta$  scan is shown in Figure 9. The central peak is from the InP substrate, and the peaks on the left and right are from epitaxial layers. Information about the lattice constant and composition of epitaxial layers can be extracted from this plot. For a coherently tensile strained epitaxial layer, the in-plane lattice constant ( $d_{\parallel}$ ) of the layer is the same as the substrate, but the lattice constant perpendicular to the surface ( $d_{\perp}$ ) is shorter than the bulk equilibrium lattice constant, in order to maintain Poisson's ratio. It is this ' $d_{\perp}$ ' that is measured from the x-ray diffraction data. Thus, the peak from such a layer is seen to the right of the substrate peak. The reverse is true for an epitaxial layer under coherent compressive strain.

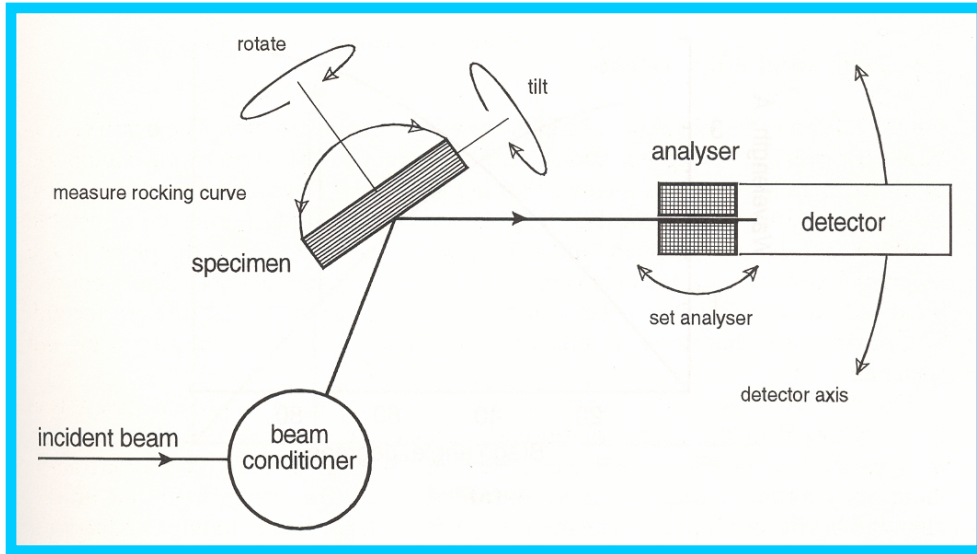


Figure 8. X-ray diffraction setup. Adapted from [43].

X-ray simulation software, such as BEDE Rads Mercury, can be used fit the simulated model to the measured diffraction data. Detailed information about the composition and thicknesses of layers and interfaces can be obtained using such fitting software. In Figure 9, the black curve shows the experimentally measured data, and the red curve shows the simulated data. Excellent agreement between the experimental and simulated data can be achieved for most structures.

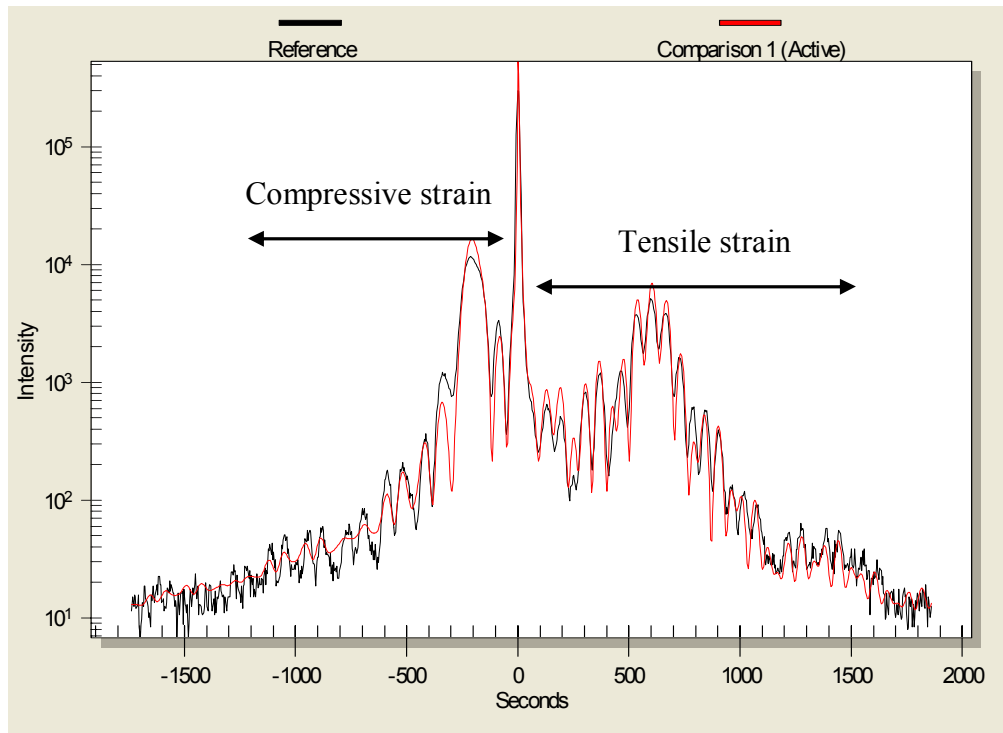


Figure 9. Measured (black) and simulated (red) x-ray rocking curves.

### 3.3 MBE GROWTH OF MIXED GROUP-V MATERIALS

Group III – Arsenide -Antimonides are interesting III-V alloys, and hold much promise for heterojunction transistors and mid-IR communication devices. On GaAs substrates,  $\text{GaAs}_y\text{Sb}_{1-y}$  has been shown to emit at  $1.3\mu\text{m}$  using strained quantum wells [44]. On InP substrates, lattice matched  $\text{Al}_{1-x}\text{Ga}_x\text{As}_y\text{Sb}_{1-y}/\text{GaAs}_y\text{Sb}_{1-y}$  provide high refractive index step materials for DBR mirrors, offering a much needed improvement over  $\text{Ga}_x\text{In}_{1-x}\text{As}_y\text{P}_{1-y}/\text{InP}$ [45].

The control of the group-III mole fraction in the MBE growth of mixed III-V materials is fairly straightforward. However, group-V composition control is not so. MBE growth is normally carried out under a group-V overpressure, i.e. V/III ratio  $> 1$ . Under these conditions, the sticking coefficient of group-III atoms is very close to unity. However, the group-V atoms of different species have to compete for a limited number of anion sites. This leads to a strong dependence of the alloy composition on the growth conditions. Antimony incorporation in III-AsSb is strongly dependent on the various growth parameters, namely, substrate temperature, group III growth rates, and Arsenic and Antimony beam equivalent pressures (BEPs). This dependence was studied by growing  $\text{GaAs}_y\text{Sb}_{1-y}$  as strained QWs on GaAs [40], and  $\text{AlAs}_y\text{Sb}_{1-y}$  bulk layers on InP. The layer compositions of GaAsSb strained QWs on GaAs were determined by room temperature PL. The same could not be done for AlAsSb layers on InP, since AlAsSb is an indirect bandgap material. Therefore x-ray diffraction was used to determine the composition of AlAsSb bulk layers on InP. A schematic structure of the samples grown for x-ray diffraction is shown in Figure 10. AlAsSb layers were grown on thin GaInAs or AlInAs buffer layers on the substrate, and were capped with a thin GaInAs layers to prevent oxidation of AlAsSb in air.

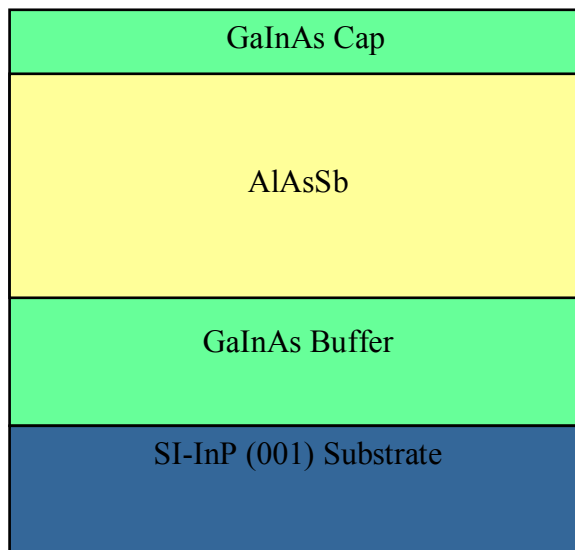


Figure 10. Schematic structure of an x-ray sample.

### 3.3.1 Sample Preparation

All semiconductor substrates form a thin native oxide on the surface when exposed to air. The thickness of the oxide depends on the substrate and the amount of time it is exposed to air. Even when care is taken to keep the substrate sealed in non-oxidizing environments, some oxidation takes place. Therefore it is important to remove this oxide before starting epitaxial growth on the substrate. In the MBE technique, it is common practice to thermally desorb the oxide from the surface of the substrate in-situ just before starting film growth. This process is called 'de-ox'. InP substrates can be 'de-oxed' between 480°C and 560°C, depending on the age of the substrate and the type and amount of group-V flux used. If the substrate is heated without sufficient group-V flux, Phosphorous starts



to desorb from the surface above 350°C and Indium droplets form on the surface making it useless for high-quality growth. InP substrates can be ‘de-oxed’ under both As and P flux. The ‘de-ox’ recipe is generally reactor specific.

For the structures reported in this dissertation, the substrates were heated under  $1.5 \times 10^{-5}$  torr of Arsenic BEP to 560°C. At this temperature, the RHEED pattern changed from a 2x2 to 2x4, as shown in Figure 11. The substrate temperature was independently monitored by an infrared pyrometer.

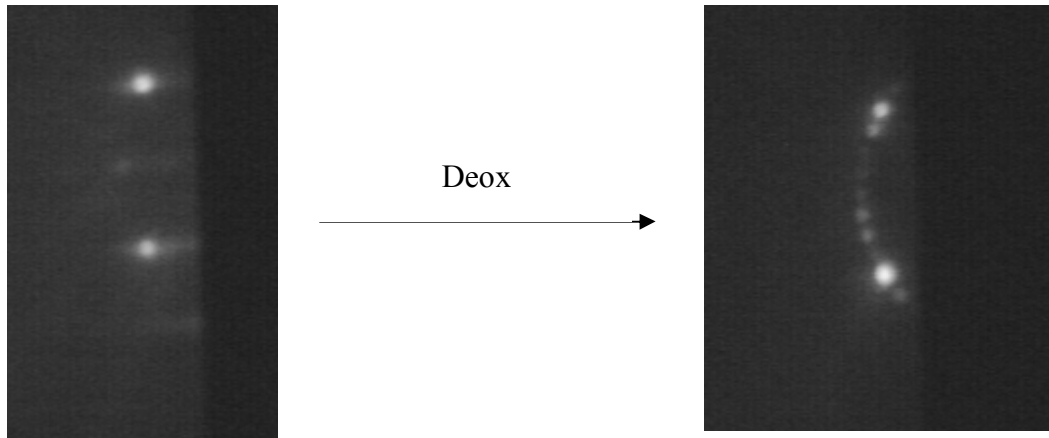


Figure 11. RHEED patterns before (2x2) and after de-ox (2x4).

While ramping the substrate temperature from room temperature up to the de-ox temperature, a fairly rapid ramp rate is used (20°/min – 50°/min). Exposing the InP substrate to Arsenic flux for long periods of time can result in InAs formation on the surface which effects the quality of the material grown subsequently [46].

### **3.3.2 Effects of Growth Parameters on Antimony Incorporation**

It is important to maintain accurate control over the composition of the layers being grown in order for the devices to operate within the defined parameters. The composition of GaAsSb used in the absorption regions of photodiodes not only determines the wavelength of operation, but also has an influence on the crystal quality. Any significant deviations from the lattice matched composition ( $\text{GaAs}_{0.51}\text{Sb}_{0.49}$ ) can result in increased defects and higher dark current from the device. For photodiodes that use strain-compensated layers, accurate composition control ensures that the net strain in the device is maintained below the critical value in order to avoid dislocations and other defects.

As explained above, the composition of GaAsSb or AlAsSb grown under a group-V overpressure depends on the growth temperature, group-III growth rate, and the group-V fluxes (Arsenic and Antimony). We ran experiments to determine the effects of these growth parameters on the composition of AlAsSb. The trends found in this study can be directly translated to the growth of GaAsSb on InP. Similar trends were found for the growth of strained GaAsSb on GaAs substrates [40] For the samples grown for this study, only one parameter was varied at a time while the others were carefully kept constant.

#### ***3.3.2.1 Growth temperature***

To determine the effect of temperature, samples were grown at 500°C, 515°C, and 530°C. The Arsenic and Antimony BEPs were fixed at  $3.0 \times 10^{-6}$  torr

for each of these samples, and the Aluminum growth rate was 0.8 monolayers/second. The (004) XRD data from these samples is shown in Figure 12. The AlAsSb peaks are shown with arrows for the structures grown at 500°C and 530°C. For the structure grown at 515°C, the layer was perfectly lattice-matched; hence the AlAsSb layer peak coincides with the InP substrate peak. We observed that with increasing growth temperature, the Antimony incorporation in the film decreases, because of increased Sb desorption from the substrate at higher growth temperatures. The compositions of these layers were determined using Bede Rads Mercury simulation software.

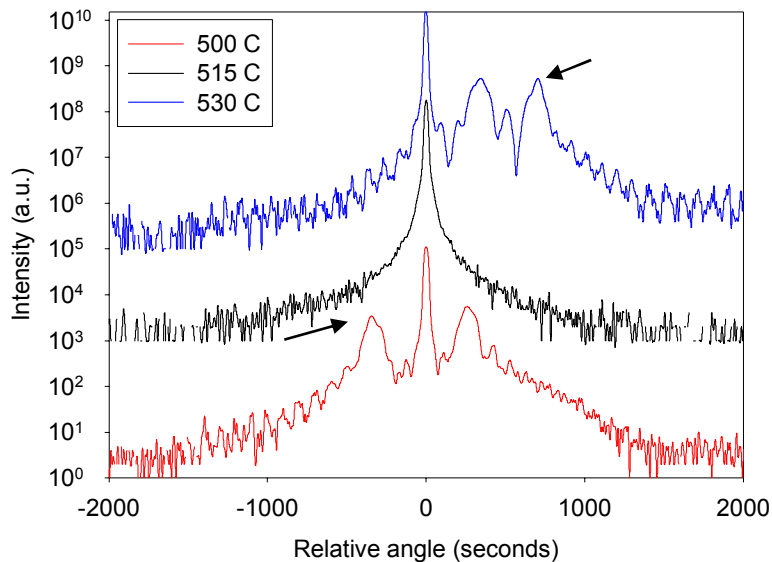


Figure 12. X-ray diffraction data from samples grown at three different temperatures.

The rate of change of composition with temperature was found to be about  $0.0017/^\circ\text{C}$ . This number is expected to change for different growth rates and Arsenic/Antimony fluxes.

### 3.3.2.2 Group-III growth rate

Antimony incorporation was also seen to increase with increasing group-III growth rate. XRD data from samples grown at different Aluminum growth rates is shown in Figure 13. All of these samples were grown at  $500^\circ\text{C}$  and at Arsenic and Antimony BEPs of  $3.0 \times 10^{-6}$  torr. The increased Antimony incorporation with higher Aluminum growth rate suggests that at higher group-III growth rates, there are more cations available for Sb adatoms to bond with, which keeps the Sb atoms from desorbing from the surface.

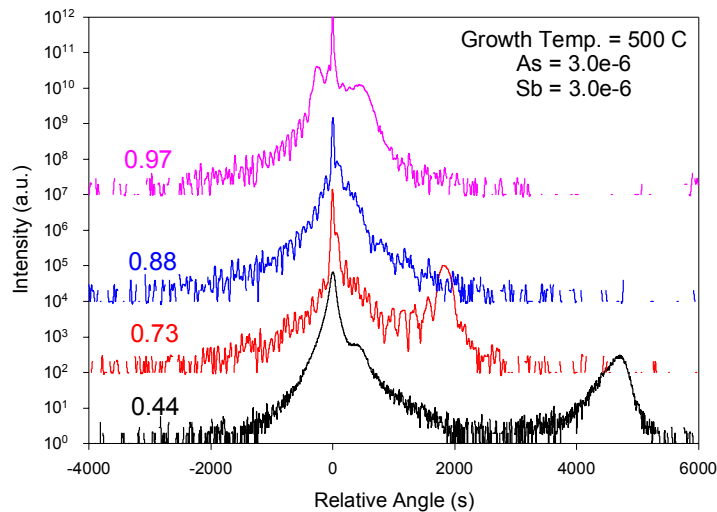


Figure 13. XRD data from samples grown at different group-III growth rates

### 3.3.2.3 Group-V flux

For the growth of both GaAsSb and AlAsSb, Arsenic seemed to incorporate preferentially over Antimony. At a high As BEP of  $6.0 \times 10^{-6}$  torr, a change in Sb BEP produced little change in Sb incorporation in the film, whereas, at a lower As BEP of  $3.0 \times 10^{-6}$  torr, a similar change in Sb BEP produced a larger change in Sb incorporation. The same is also evident from the observation that increasing the As and Sb BEPs while keeping the As/Sb BEP ratio fixed at 1.0 resulted in a decreased Sb incorporation. The XRD data from three samples grown under different Arsenic and Antimony BPEs is shown in Figure 14.

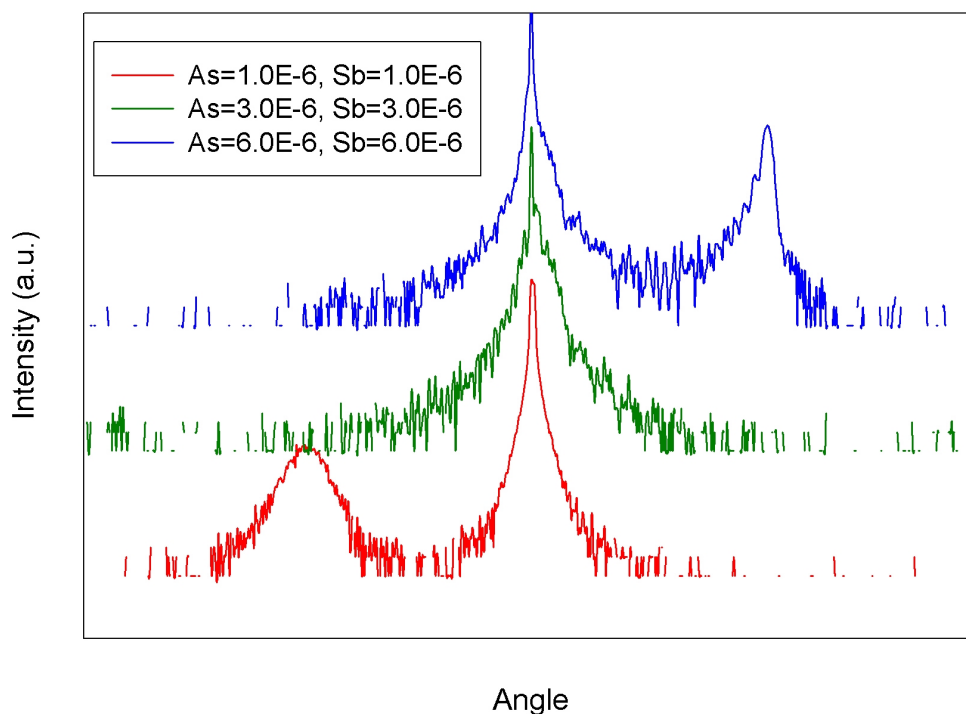


Figure 14. XRD data from samples grown with equal Arsenic and Antimony BEPs.

For these samples, the Arsenic/Antimony BEP ratio was maintained at one, and all other growth parameters were maintained constant. Figure 15 shows the effect of Arsenic BEP on the layer composition, for a fixed Antimony BEP of  $3.0 \times 10^{-6}$  torr.

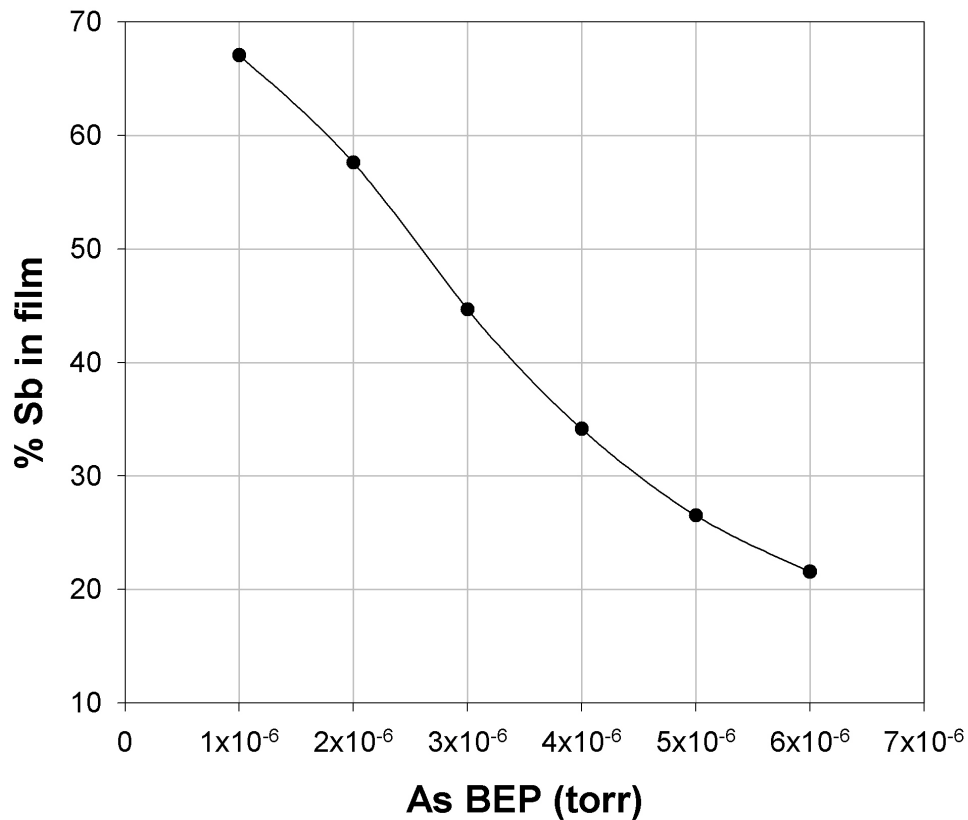


Figure 15. Effect of Arsenic BEP on the composition of AlAsSb, for Antimony BEP =  $3.0 \times 10^{-6}$  torr.

Optimal growth temperature was determined by comparing the PL intensity and peak width of samples grown at different temperatures. For both

strained GaAsSb on GaAs, and lattice-matched GaAsSb on InP, the optimal growth temperature was found to be about 530°C. Further growth optimizations are possible and will be discussed in the Chapter 7. A lower growth temperature of about 515°C, under a different set of As and Sb flux conditions may lead to better crystal quality.

### **3.4 DEVICE FABRICATION**

After determining the parameters for MBE growth of GaAsSb, we grew photodiode structures incorporating the GaInAs-GaAsSb type-II quantum wells. These wafers were fabricated into top-illuminated mesa devices using a H<sub>3</sub>PO<sub>4</sub>:H<sub>2</sub>O<sub>2</sub>:H<sub>2</sub>O (1:1:10) wet-chemical etch. The mesas were then passivated by plasma-enhanced chemical vapor deposition (PECVD) of 2000 Å of SiO<sub>2</sub> at 285°C. Ti-Pt-Au metal ring contacts were deposited on the top surface of the mesa for p-contacts, and AuGe-Ni-Au contacts were deposited on the n-surface. Conventional photolithography and lift-off metallization techniques were used to define the metal contacts. Au microwave contact pads were fabricated for wire bonding. The n-pads were deposited directly on the n-contact metal. P-pads were deposited on SiO<sub>2</sub>, and were connected to the p-contacts by an air bridge. The air bridge was deposited using electro-deposition of Au. Wire bonding was used to contact the devices.

### 3.5 SUMMARY

Molecular beam epitaxy (MBE) was used to grow the material and devices for the research presented in this dissertation. Composition of MBE grown mixed group-V materials depends on the growth parameters; i.e. the growth temperature, the growth rate, and the group-V fluxes. These dependencies were studied for the growth of III-AsSb on InP substrates. The Antimony incorporation decreased with increasing growth temperature and decreasing group-III growth rate. Arsenic BEP seemed to have a greater effect on the composition than the Antimony BEP. Good quality GaAsSb layers were grown at 525°C – 530°C, under Arsenic and Antimony BEPs of  $3.0 \times 10^{-6}$  torr.



## **Chapter 4 Photodiode Characterization**

### **4.1 INTRODUCTION**

Many different figures of merit are available to quantify the performance of photodiodes. Different characterization techniques may be used to measure the device performance and the choice depends on the type of device and the application. The figures of merit used in this dissertation are defined in this chapter, along with descriptions of the test apparatus and measurement techniques.

### **4.1 P-I-N AND AVALANCHE PHOTODIODES**

A p-i-n photodiode is formed by placing an intrinsic (or lightly doped) absorption region between highly doped p- and n- layers. On applying reverse bias to this type of p-i-n (p-p<sup>-</sup>-n or p-n<sup>-</sup>-n) photodiodes, most of the electric field is in the intrinsic layer. The electron-hole pairs generated in this layer drift to the n- and p- layers respectively, and current flows through the device. Several other mechanisms apart from light absorption may be responsible for electron-hole pair generation, and will be discussed in the subsequent sections.

In the simplest case, a high reverse bias applied to a p-i-n photodiode can produce a sufficiently high electric field in the intrinsic region to cause impact ionization of electrons and/or holes. These secondary electrons and holes may further impact-ionize to create still more electron-hole pairs. This avalanche effect produces many extra electron-hole pairs for every primary electron or hole and

causes multiplication of the primary current. This multiplication process does not distinguish between photo-generated carriers and dark-carriers.

There are some drawbacks to applying a high bias across a p-i-n device to achieve gain. Under high electric fields, band-to-band tunneling of carriers may cause high dark current [47]. This can swamp the photo-generated signal. Avalanche process is also a statistical process and has some noise associated with it. When both electrons and holes are allowed to multiply, the avalanche noise is significantly increased [48].

The well designed separate absorption, charge, and multiplication (SACM) structure solves both of the above problems by separating the low bandgap absorption region from a high bandgap multiplication region [49]. A thin, lightly-doped charge region insures a low electric field in the absorption region to avoid tunneling. At the same time, a high electric field in the wide-bandgap multiplication region causes avalanche gain without accompanied tunneling. In this structure, only one type of carrier is injected from the absorption region to the multiplication region. Thus multiplication noise is significantly reduced.

### **4.3 DC CHARACTERIZATION**

The I-V characteristics of the devices were measured using HP 4145B or Agilent 4156B semiconductor parameter analyzer. The room temperature photocurrent data was taken under white light illumination provided by a microscope light. While measuring the dark current at various temperatures, the

photodiodes were placed in a cryostat and the cryostat windows were covered with Aluminum foil to prevent any light from entering the cryostat. A cold shroud around the device helped minimize stray infrared radiation incident on the device.

The dark current from a device depends on the size of the device. Therefore, it is customary to report the dark current density instead of the actual dark current. The shunt resistance ( $R_0$ ) of a diode can be determined by calculating the resistance from the low bias ( $\pm 1V$ ) I-V data. High shunt resistance implies low leakage current from the device. Another figure of merit routinely used to report MWIR photodiode performance is the  $R_0A$  product (shunt resistance - area product.)

Avalanche gain of a device at a certain bias voltage can be calculated using the following relation:

$$M(V) = \frac{I_{ph}(V) - I_d(V)}{I_{ph}(unity) - I_d(unity)} \quad \dots 4.1$$

In the above equation,  $M(V)$  is the gain at a certain applied voltage  $V$ ,  $I_{ph}(V)$  and  $I_d(V)$  are the photo and dark-currents at voltage  $V$ , and  $I_{ph}(unity)$  and  $I_d(unity)$  are the photo and dark-currents at unity gain.

In the case of some SACM APDs, the unity gain point may not be available. This happens when there is some gain at the punchthrough voltage. In such cases, the gain at punchthrough can be determined by comparing the photo-current from the APD to the unity gain photo-current of a p-i-n device under the

same illumination. The p-i-n photodiode must have exactly the same absorption region as the APD to get accurate gain values.

#### 4.4 DARK CURRENT

The three primary mechanisms that contribute to the dark generation of carriers in a reverse biased photodiode are diffusion, thermal generation and tunneling [47, 50]. Expressions for each of these components appear below:

$$J_{dark} = J_{diff} + J_{G-R} + J_{tun} \quad \dots 4.2$$

$$J_{diff} = qn_i^2 \left[ \frac{D_n}{L_n N_a} + \frac{D_p}{L_p N_d} \right] (e^{qV/kT} - 1) \quad \dots 4.3$$

$$J_{G-R} = \frac{qn_i W}{\tau} (e^{qV/kT} - 1) \quad \dots 4.4$$

$$J_{tun} = \frac{q^3 E_m V}{4\pi^2 \hbar^2} \sqrt{\frac{2m_t}{\epsilon_g}} \cdot \exp\left(\frac{-4\sqrt{2m_t \epsilon_g^3}}{3q\hbar E_m}\right) \quad \dots 4.5$$

The symbols used in the above expressions are explained in the table below:

Symbol	Description
$J_{dark}$	Total dark current density
$J_{diff}$	Diffusion current density

$J_{G-R}$	Current density from thermal generation-recombination in the intrinsic region
$J_{tun}$	Tunneling current density
$q$	Electronic charge, $1.6 \times 10^{-19}$ Coulomb
$T$	Temperature, Kelvin
$k$	Boltzmann's constant, $1.38 \times 10^{-23}$ J/K
$N_d, N_a$	Donor and acceptor concentrations
$L_n, L_p$	Electron and hole diffusion lengths
$D_n, D_p$	Electron and hole diffusion coefficients
$n_i$	Intrinsic carrier concentration
$\tau$	Minority carrier lifetime
$V$	Applied bias
$W$	Depletion width
$E_m$	Maximum electric field
$\epsilon_g$	Bandgap
$m_t$	Tunneling effective mass
$h$	Planck's constant, $6.6 \times 10^{-34}$ J-s

The diffusion component of the dark current is generally very small and is negligible as compared to the other two components. The thermal generation-recombination current has a large dependence on temperature. This mechanism is dominant at low bias and high temperatures. The activation energy for thermal generation can be calculated from the slope of the line between dark current (on

natural log scale) and  $1/T$ . The thermal generation can take place through mid-gap traps. The traps have some energy distribution in the bandgap and the activation energy generally points to the average energy of all the traps.

Tunneling current has a very small dependence on temperature which comes from the change in bandgaps with temperature [26]. Tunneling can be from band-to-band or trap-assisted [50].

#### **4.5 SPECTRAL RESPONSE**

It is important to know what wavelengths of light the photodiode absorbs and how efficiently it absorbs them. The spectral response of the devices reported in this dissertation was measured using a Nicolet Magna-II Fourier transform infrared (FTIR) spectrometer. The FTIR spectrometer forms an interferogram from a broadband light source and shines it on the photodiode [25]. The output current from the photodiode was amplified using a Stanford Research Systems (SRS) 570 current pre-amplifier. Fourier transform analysis of this signal gives the spectral response of the device. Figure 16 shows a schematic diagram of the FTIR spectrometer. A PbS detector of known responsivity was used to calibrate the FTIR source. The calibration was checked with a second, calibrated Judson technologies long-wavelength GaInAs detector.

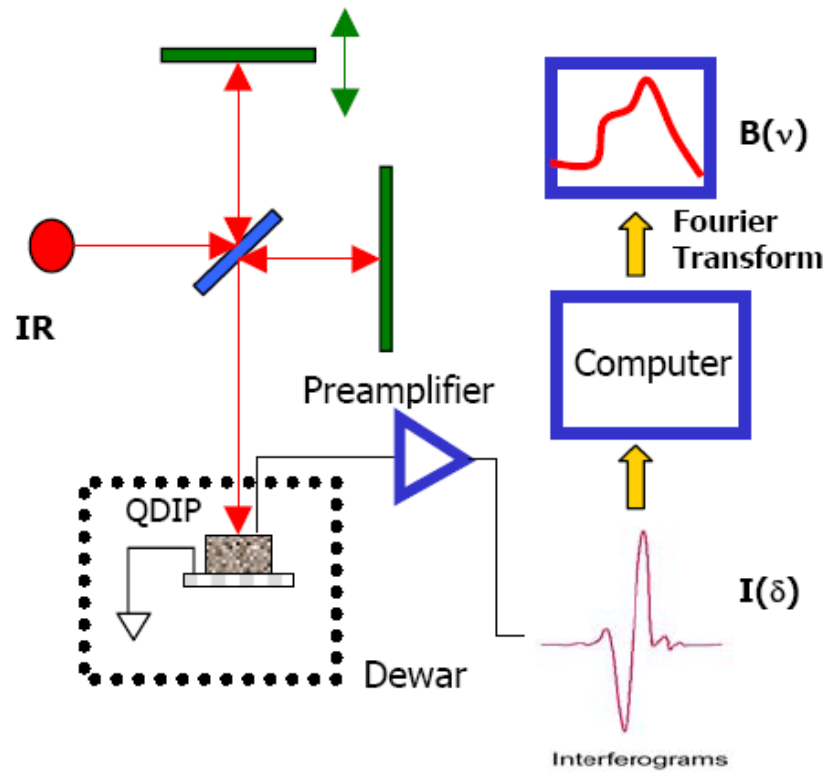


Figure 16. Principle of FTIR operation [25].

#### 4.5.1 Responsivity and Quantum Efficiency

The external quantum efficiency ( $\eta_{EQE}$ ) of the device is the ratio of the number of photons absorbed in the device to the number of incident photons. It is related to the absorption coefficient ( $\alpha$ ) and the surface reflectivity ( $r$ ) as follows:

$$\eta_{EQE} = (1 - r)[1 - e^{-\alpha d}] \quad \dots 4.6$$

The quantum efficiency is a dimensionless number and is generally reported at a certain wavelength. The responsivity of a photodiode is defined as the current produced in the photodiode per unit power of incident light. It is reported as a function of wavelength, in units of amperes per watt. The relation between external quantum efficiency and responsivity (R) at a given wavelength ( $\lambda$ ) is:

$$\frac{R(\lambda) \cdot hc}{\lambda \cdot q} = \eta_{EQE}(\lambda) \quad \dots 4.7$$

The absolute responsivity was measured by placing the photodiodes in front of a blackbody source held at 900°C. The radiation from the blackbody at temperature (T), is given by Planck's radiation law:

$$N(\lambda, T) := \frac{2 \cdot \pi \cdot h \cdot c^2}{\lambda^5} \cdot \frac{1}{e^{\frac{hc}{k \cdot T \cdot \lambda}} - 1} \quad \dots 4.8$$

The signal from the blackbody was modulated at a frequency of 140 Hz using a chopper. The power from the blackbody (at temperature T<sub>2</sub>) less radiation from the chopper (at temperature T<sub>1</sub>), in the interval  $\lambda_1 - \lambda_2$  is:

$$M(\lambda_1, \lambda_2) := \int_{\lambda_1}^{\lambda_2} N(\lambda, T_2) d\lambda - \int_{\lambda_1}^{\lambda_2} N(\lambda, T_1) d\lambda \quad \dots 4.9$$



The power incident on the device is given by:

$$P_{\text{inc}} := M(\lambda_1, \lambda_2) \cdot \frac{\pi \cdot D_{\text{ap}}^2}{4 \cdot \pi \cdot d^2} \cdot T_{\text{ZnSe}} \cdot A_{\text{det}} \quad \dots 4.10$$

In equation 4.10,  $D_{\text{ap}}$  is the aperture on the blackbody source,  $d$  is the distance between the photodiode and the blackbody,  $T_{\text{ZnSe}}$  is the transmission of the window, and  $A_{\text{det}}$  is the active area on the device mesa top.

The total current from the photodiode was measured using a current pre-amplifier and a FFT spectrum analyzer. Figure 17 shows the test apparatus. Total blackbody responsivity was calculated by dividing this current by the incident power, from equation 4.10. The responsivity as a function of wavelength was determined numerically from the spectral response curve, by calculating the contribution of each wavelength step ( $\Delta\lambda$ ) to the total responsivity. Matchcad 11 code used in the above calculation is provided in Appendix A.

External quantum efficiency as a function of wavelength was calculated from responsivity using equation 4.7.

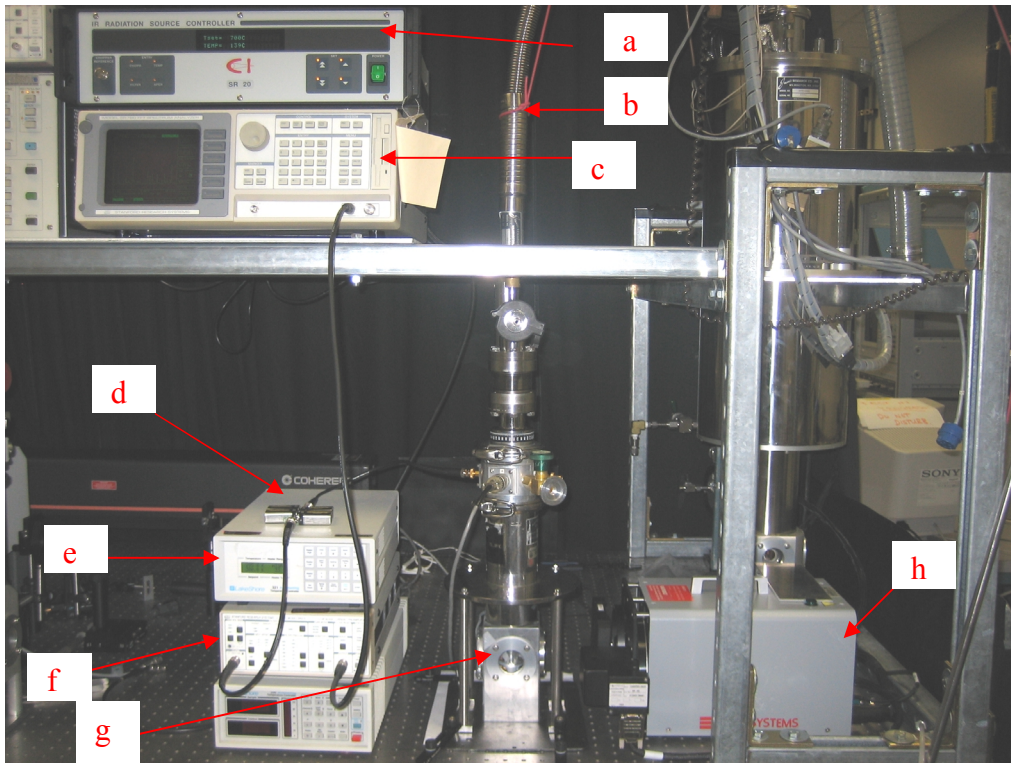


Figure 17. Blackbody responsivity measurement apparatus. a: blackbody controller; b: Liquid nitrogen tube to the cryostat; c: Stanford Research Systems FFT spectrum analyzer; d: batteries used to bias the APD; e: Lakeshore temperature controller; f: Stanford Research Systems 570 current pre-amplifier; g: Cryostat with device mounted inside; h: blackbody source

## 4.6 NOISE

Random fluctuation in current from the detector leads to noise in the signal. Low noise level is necessary for high detector sensitivity. The two main sources of noise in photodetectors are:

1. Thermal noise: All resistive elements at temperatures above zero Kelvin have thermal noise given by:

$$\langle i_{thermal}^2 \rangle = \frac{4kT}{R} B \quad \dots 4.11$$

where  $k$  is the Boltzmann's constant,  $T$  is the temperature,  $R$  is the resistance and  $B$  is the measurement bandwidth.

2. Shot noise: This originates from the random thermal generation of carriers in the intrinsic region of the photodiode. Shot noise is given by:

$$\langle i_{shot}^2 \rangle = 2eIB \quad \dots 4.12$$

In avalanche photodiodes, the total current is multiplied by the gain ( $M$ ), therefore the shot noise term scales with the square of the gain. However, in addition to this, there is extra noise contribution from the random statistical nature of the avalanche process. This excess noise factor is denoted by  $F(M)$ , and is a function of the gain [51]. The excess noise factor can be mathematically related to the gain and the ratio of electron and hole ionization coefficients by:

$$F(M) = k_{eff}M + (1 - k_{eff})\left(2 - \frac{1}{M}\right) \quad \dots 4.13$$

Where M is the avalanche gain and  $k_{eff}$  is the ratio of the electron ionization coefficient ( $\alpha$ ) and the hole ionization coefficient ( $\beta$ ).

Thus, the total noise current in an avalanche photodiode equals:

$$\langle i_n^2 \rangle = \langle i_{thermal}^2 \rangle + \langle i_{av}^2 \rangle = \frac{4kT}{R}B + 2e(I_{ph} + I_B + I_D)BM^2F \quad \dots 4.14$$

Since all the current gets multiplied by the same factor, the photo current ( $I_{ph}$ ), background diffusion current ( $I_B$ ) and the dark current ( $I_D$ ) figure in the above equation.

The excess noise from the avalanche photodiodes can be reduced by either choosing a material with a low ‘k’ value [52, 53], or by using thinner or specially engineered low-noise multiplication layers [54-56]. In these cases, the multiplication noise is reduced by making the avalanche process more deterministic.

#### 4.6.1 Detectivity

The dark current noise of the device was measured using the same procedure as the responsivity. The device was enclosed in a cold shroud to minimize stray radiation incident on the device. The noise current from the device was amplified using a pre-amplifier. An FFT spectrum analyzer was used to view

the noise current spectra. The specific detectivity was calculated from the noise current and the responsivity, using the following equation:

$$D^*(\lambda) = \frac{R(\lambda) \cdot \sqrt{A_{\text{det}}}}{i_{\text{noise}}} \quad \dots 4.15$$

$D^*(\lambda)$  is the specific detectivity (in  $\text{cm Hz}^{1/2} \text{ W}^{-1}$ ) as a function of wavelength,  $R(\lambda)$  is the responsivity,  $A_{\text{det}}$  is the active area of the device on the mesa top, and  $i_{\text{noise}}$  is the noise current measured at the modulation frequency used in responsivity measurement (140 Hz).

## Chapter 5 GaInAs-GaAsSb *p-i-n* Photodiodes

### 5.1 INTRODUCTION

The band lineup between GaInAs and GaAsSb was discussed in Chapter 2. Based on our initial calculations using The Model Solid Theory [57], we expected the effective type-II bandgap between Ga<sub>0.47</sub>In<sub>0.53</sub>As and GaAs<sub>0.51</sub>Sb<sub>0.49</sub> to be about 490 meV (corresponding to 2.5 $\mu$ m). After developing the MBE growth procedure for good quality GaAsSb growth on InP, as discussed in Chapter 3, we fabricated *p-i-n* photodiodes with type-II QWs in the intrinsic region. This chapter discusses the device structure and results from these *p-i-n* photodiodes.

### 5.2 THE P-I-N STRUCTURE

In *p-i-n* photodiodes, the undoped absorbing region is placed between *p*-type and *n*-type layers. A schematic of the device structure is shown in Figure 18. In the case of most MBE grown III-V *p-i-n* diodes, the intrinsic regions are unintentionally *n*-type doped ( $\sim 10^{15}$  cm<sup>-3</sup>). When this structure is reverse-biased, the intrinsic region is depleted at a low bias and most of the voltage is dropped across it. The incident photons get absorbed in the intrinsic region creating electron-hole pairs. These carriers then drift to the doped layers and are collected as photocurrent. It is generally advisable to use wide-bandgap materials for the *p*- and *n*-layers to avoid the absorption of the wavelengths of interest in these layers. *P-i-n* photodiodes can also be operated as avalanche photodiodes under high

reverse bias. However, there are certain disadvantages to this type of operation, which will be discussed in the next chapter.

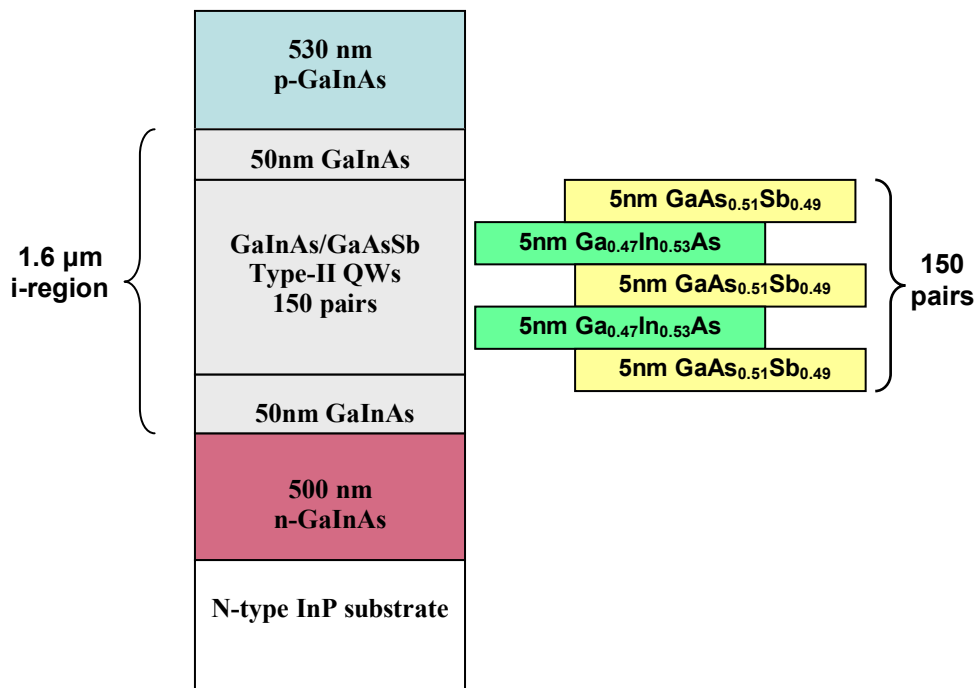


Figure 18. Schematic diagram of the p-i-n device structure.

### 5.3 MBE GROWTH

The structure shown in Figure 18 was grown on an n-type American X'tal Technology (AXT) InP (001) substrate. Before layer growth, the substrate surface was prepared following the de-ox procedure listed below:

Table 1 De-ox procedure used before p-i-n device growth.

<b>Ramp (substrate-temperature)</b>	<b>Ramp rate</b>	<b>Hold time</b>	<b>Remarks</b>
Room temperature - 500°C	50°/min	5 minutes	--
525°C	20°/min	5 minutes	Determine T <sub>g</sub>
560	20°C/min	5 minutes	2x4 RHEED pattern

Following the de-ox procedure, the substrate temperature was lowered to the growth temperature. The growth sequence from the substrate up is described below.

A 500nm thick n-type doped (Si:  $3 \times 10^{18} \text{ cm}^{-3}$ ) Ga<sub>0.47</sub>In<sub>0.53</sub>As layer was first grown to serve as a buffer layer and the n-contact layer. The intrinsic-region was grown next, and consisted of 150 pairs of un-doped Ga<sub>0.47</sub>In<sub>0.53</sub>As-GaAs<sub>0.51</sub>Sb<sub>0.49</sub> type-II quantum wells. Each layer in the absorption region was 5nm thick. Following the i- region, a 500nm thick p-type doped (Be:  $3 \times 10^{18} \text{ cm}^{-3}$ ) Ga<sub>0.47</sub>In<sub>0.53</sub>As layer was grown. Finally thin, highly p-type doped (Be:  $3 \times 10^{19} \text{ cm}^{-3}$ ) Ga<sub>0.47</sub>In<sub>0.53</sub>As layer formed the p-contact layer.

Between the growth of each Ga<sub>0.47</sub>In<sub>0.53</sub>As layer and GaAs<sub>0.51</sub>Sb<sub>0.49</sub> layer in the i-region, the Arsenic and Antimony beam equivalent pressures (BEPs) need to be changed by changing the openings of the valved-crackers. This process usually takes 4 to 5 seconds. For this reason, 10 second interrupts were used between the growths of successive Ga<sub>0.47</sub>In<sub>0.53</sub>As and GaAs<sub>0.51</sub>Sb<sub>0.49</sub> layers. This



interrupt time allows the flux to stabilize to the value required for the next layer, and also allows any floating layers of group-V flux from the previous layer to be replaced by the appropriate group-V flux for the next layer [40]. These interrupts, and changing the group-V flux in general, cause some anion exchange at the interfaces. The anion exchange in turn has a bearing on the composition, quality and abruptness of the interfaces. Sharp and high quality interfaces are important to keep the dark current of the device low. Further optimization of interfaces is possible, and may lead to increased detectivity of these photodiodes. This issue is discussed further in Chapter 7.

The entire structure was grown at a temperature of 525°C. Arsenic flux of  $1.5 \times 10^{-5}$  torr was used during de-ox and during the growth of the  $\text{Ga}_{0.47}\text{In}_{0.53}\text{As}$  layers. During the growth of  $\text{GaAs}_{0.51}\text{Sb}_{0.49}$  layers, both Arsenic and Antimony BEPs were set to  $3 \times 10^{-6}$  torr.

During the growth of any layer that has a narrower bandgap than the substrate, the substrate temperature increase due to the absorption of additional radiation from the heater. This temperature increase is quite insignificant for the growth of most III-V compounds. However, during the growth of mixed group-V alloys, when the composition is very growth-temperature sensitive; this small increase in temperature can result in a compositional grading of the layers. No attempts were made to counter the above described increase in temperature for the devices discussed in this dissertation. However, in principle, it is possible to calculate the rate of increase of temperature with narrow bandgap layer growth, and to adjust the substrate temperature accordingly.

## **5.4 DEVICE RESULTS**

After wafer growth, mesa devices were fabricated as described in Chapter 3. The results from electrical and optical characterization of these devices are presented below.

### **5.4.1 DC characteristics**

HP 4145B and Agilent 4156C semiconductor parameter analyzers were used to measure the I-V characteristics of the p-i-n photodiodes. Figure 19 shows the reverse I-V from a 64 $\mu$ m diameter mesa device at different temperatures.

Room temperature dark current at -1V bias was 160 nA, corresponding to a dark current density of less than 5mA/cm<sup>2</sup>. To further understand the mechanisms contributing to the dark carrier generation, we need to determine whether the majority of the dark current is generated in the bulk of the device or at the surface. Surface contribution comes from traps that result from dangling bonds at the mesa walls, while the bulk contribution comes from thermal generation and tunneling (see Chapter 4). To reduce the surface leakage, SiO<sub>2</sub> passivation was applied to the mesa walls.

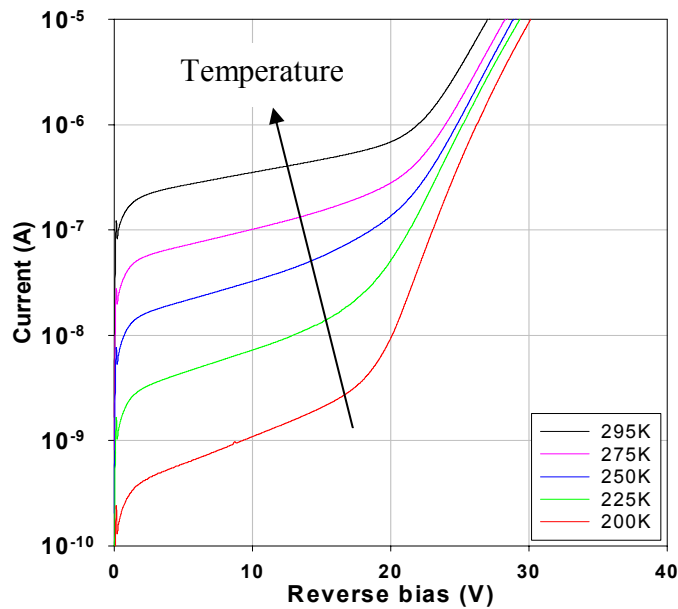


Figure 19. Reverse I-V curves from a 64 microns diameter mesa device at different temperatures.

We measured the room temperature dark current from devices of various diameters, plotted in Figure 20. The dark current vs. diameter for two different reverse bias voltages is plotted in Figure 21. As can be seen from the figure, the dark-current scales quadratically with diameter (linearly with device area), suggesting that majority of the dark-current is generated in the bulk of the device. A linear dependence of the dark current on the diameter would have suggested surface leakage.

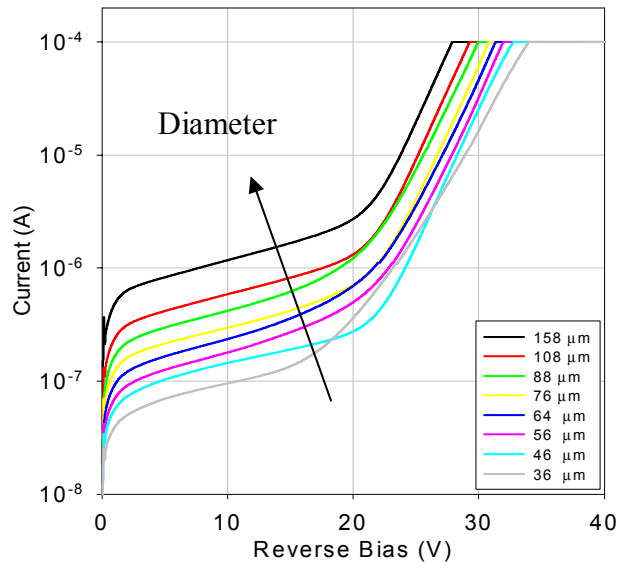


Figure 20. Room temperature dark current as a function of reverse-bias, for different diameter devices.

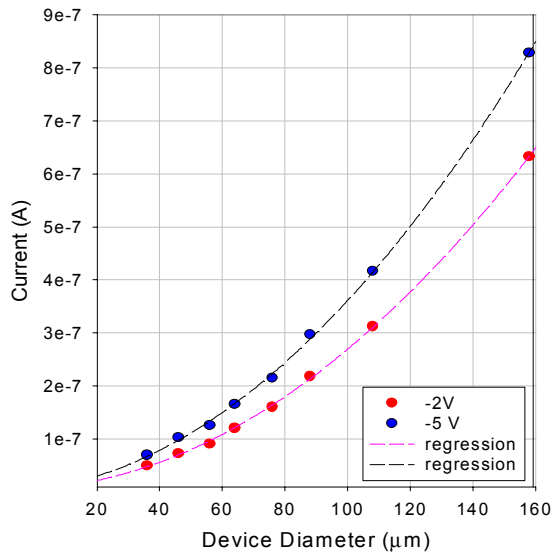


Figure 21. Room temperature dark-current vs. device diameter at two different reverse-bias voltages.

After determining that the majority of the dark-current is not originating at the device surface, the next step was to look into the mechanisms contributing to the bulk generation of dark carriers. As discussed in Chapter 4, the three primary contributors to bulk-generated dark current are diffusion, thermal generation, and tunneling. Diffusion is generally very low in reverse biased junctions. That leaves thermal generation and tunneling. It can be seen from Figure 19 that dark current at low bias drops rapidly with temperature. This suggests that the dominant mechanism for dark current in this regime is thermal generation of carriers. To further examine the mechanism of thermal generation, natural log of the dark current was plotted against the reciprocal of the temperature. The slope of a good linear fit to this data gives the activation energy for thermal generation of carrier [47]. Figure 22 shows the dark current vs.  $1/T$  at a reverse bias of 2 V and 5 V. The activation energy calculated from the slope of lines is 0.326mV and 0.318mV. These values are close to half the bandgap of both  $\text{Ga}_{0.47}\text{In}_{0.53}\text{As}$  and  $\text{GaAs}_{0.51}\text{Sb}_{0.49}$ .

This value of activation energy suggests that most of the carrier generation is through mid-gap traps (see discussion in Chapter 4.) It should be noted that the activation energies calculated in the above fashion are the averages of trap energies. The actual trap levels are distributed about this average. The thermal generation of carriers through trap levels with average energy in the middle of the bandgap of the layers is only a first order estimation of the mechanisms contributing to low bias dark current. In a structure with a complicated absorption layer such as the one in this case, with 150 layers of two different materials and

more than 300 interfaces, there are many complicated processes at play. The interfaces have a higher defect density than the layers themselves, and contribute heavily to the dark current. This is evident in comparisons of the dark current from this device with the dark-current from GaInAs homojunction p-i-n devices. Quantitative analysis of defect states in the interfaces is an interesting, yet challenging problem, and will be dealt in the future work section of Chapter 7.

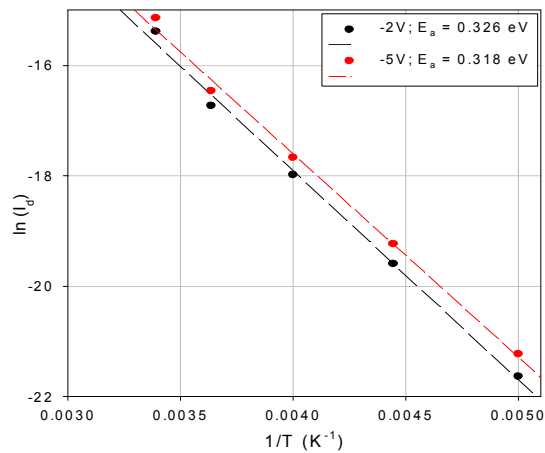


Figure 22. Plot of log of the dark current vs.  $1/T$  at two different reverse bias voltages.

At high reverse bias, the dark current has a small dependence on temperature, which suggests that the dark current at high electric fields is dominated by tunneling. There are multiple tunneling mechanisms that may be contributing to the high-field dark current. These include direct band-to-band tunneling, defect assisted tunneling, and tunneling across the type-II interfaces.

While it will be very interesting to understand these mechanisms, it is much easier to simply minimize the contribution of tunneling to the dark-current by limiting the electric field in the arrow bandgap region. The separate absorption, charge, and multiplication (SACM) structure allows accurate control over the electric fields in the absorption and multiplication layers of an APD. In such a structure, it is possible to maintain a low electric field across the arrow-bandgap absorbing layer to minimize tunneling. At the same time, a high electric field in the wide bandgap multiplication layer allows avalanche gain. Chapter 6 includes a detailed discussion on the SACM structure.

Avalanche gain was not observed from the I-V curves of this device because at high fields, the tunneling current was too high. Since tunneling has a very weak dependence on temperature, going to low temperatures did not reduce the high field dark current significantly. Therefore, no multiplication gain could be measured, even at low temperatures.

Another figure of merit for photodetectors is  $R_0$  - the shunt resistance, and the  $R_0A$  product, as discussed in Chapter 3. The shunt resistance of the device is calculated from the low bias I-V data. Calculated shunt resistance and  $R_0A$  products from the device are shown in Figure 23.

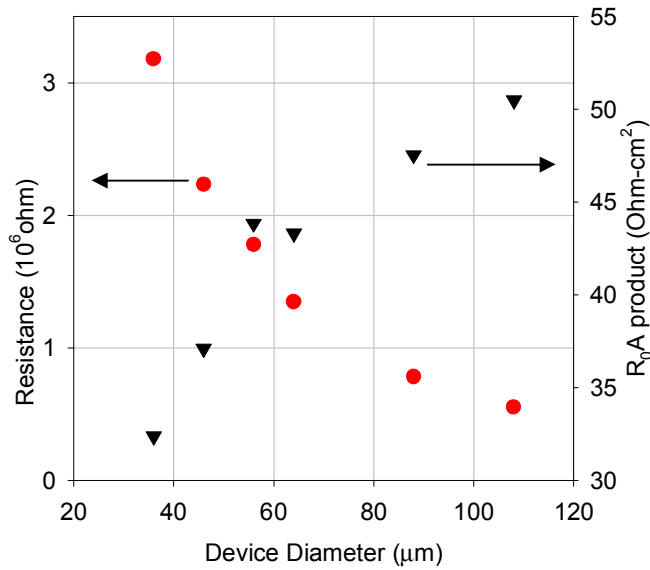


Figure 23. Room temperature shunt resistance (red circles) and  $R_oA$  product (black triangles) from different diameter devices.

### 5.4.2 Optical characterization

A Nicolet Magna-II Fourier transform infrared (FTIR) spectrometer and a Stanford Research Systems (SRS) 570 low-noise current preamplifier were used to measure the spectral response of the device at different temperatures and bias conditions. The device was loaded in a cryostat fitted with a ZnSe window. The ZnSe window has a flat transmission curve for the infrared spectrum of interest for these measurements ( $1\mu\text{m}$  to  $3\mu\text{m}$ ). The FTIR spectrometer's internal 'white' light source was used to illuminate the device. In an ideal case, the device-under-test must be illuminated with broadband signal whose intensity vs. wavelength curve is totally flat. The broadband light from the 'white' source does not have



uniform intensity as a function of wavelength. Therefore the measured response from the device being tested must be corrected using the ‘white’ source spectral intensity data. The relative spectral intensity of the ‘white’ source was determined by measuring this source with a calibrated PbS detector. Using the measured response from the PbS detector and its known responsivity, the spectral intensity of the white source was calculated according to:

$$I(\lambda) = \frac{i_{measured}(\lambda)[A]}{R_{known}(\lambda)[A/W]} \quad \dots 5.1$$

where  $I(\lambda)$  is the intensity of the ‘white’ source,  $i_{measured}(\lambda)$  is the current from the PbS detector, and  $R_{known}(\lambda)$  is the known responsivity of the PbS detector. The spectral intensity of the ‘white’ source was independently verified using a calibrated Judson Technologies long-wavelength GaInAs detector, using the same procedure described above. The intensity curves from the two methods agreed closely.

The normal incidence photo-response spectra measured at various temperatures and at -2V reverse bias are shown in Figure 24. The data at each temperature is normalized to the maximum value at the same temperature. The type-I (spatially direct) peaks from  $Ga_{0.47}In_{0.53}As$  and  $GaAs_{0.51}Sb_{0.49}$  QWs are seen at about  $1.5\mu m$  and the type-II (spatially indirect) response is seen from  $1.7\mu m$  to  $2.5\mu m$ . This is within experimental error of the calculated type-II band-gap shown in Chapter 2. As expected, the response peaks red-shift with increase in temperature, because of the reduction of the bandgaps at higher temperature. The relative response (and responsivity) increases with temperature. We believe

that this is due to photo-generated carriers having more energy to escape the QWs and transit to the electrodes.

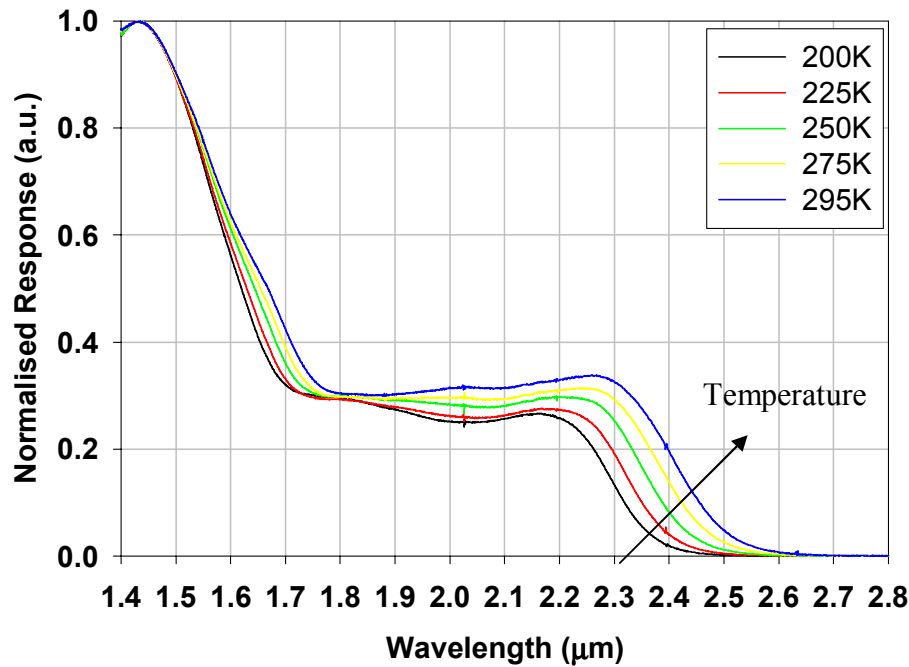


Figure 24. Spectral response from the p-i-n device measured at -2V bias and at different temperatures.

The spectral response of the device shows two peaks at about  $2.05\mu\text{m}$  and  $2.28\mu\text{m}$  at room temperature. Since these peaks are broad and not very well-defined, they can not be reliably correlated to transitions between any specific energy states in the QWs. Photoluminescence or electroluminescence data measured at low temperatures would be helpful in further understanding the relative transition probabilities for different energy states.

Spectral response measured at different reverse bias voltages, showed a 70% increase from the unbiased condition to a reverse bias of 1V. Further

increase in reverse bias did not appreciably increase the device response. The peak response wavelength did not change as a function of reverse bias.

### **5.4.3 Responsivity**

Blackbody responsivity of the device was measured using the method described in Chapter 3. The blackbody source was maintained at 900°C, and the light was chopped at a modulation frequency of 140 Hz. The output signal from the device was amplified using a low-noise current pre-amplifier and read using an FFT spectrum analyzer. A 1800nm longpass filter was placed between the blackbody source and the device to eliminate any contribution to the responsivity from direct (type-I) absorption. The responsivity and detectivity were calculated for wavelengths 1.8 $\mu$ m and longer because the KBr beam-splitter used in the FTIR spectrometer is not rated to work efficiently below about 1.8 $\mu$ m. These measured values of responsivity at different temperatures and bias conditions, along with the respective spectral response curves from the FTIR spectrometer were used to determine the absolute responsivity as a function of wavelength. The procedure for calculating responsivity and detectivity as a function of wavelength from blackbody responsivity is detailed in Chapter 3. Figure 25 shows the type-II responsivity measured at -2V bias at three different temperatures. Peak room temperature responsivity of 0.64 A/W, equivalent to 35% external quantum efficiency was observed at 2.26  $\mu$ m wavelength.

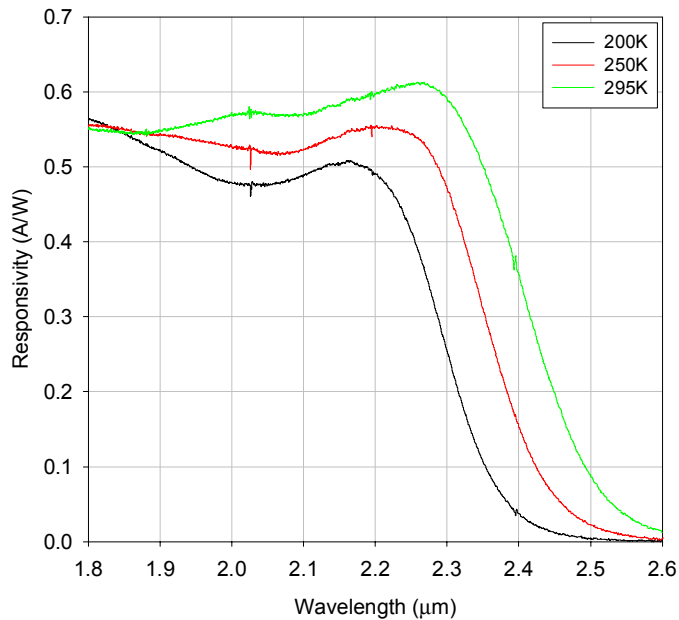


Figure 25. Responsivity vs. wavelength at three different temperatures, measured at -2V bias.

#### 5.4.4 Dark-noise and detectivity

Dark current noise was also measured from the device at different temperatures and at -2V bias. The noise was measured at 140 Hz to be consistent with the responsivity measurements. During the noise measurements, the device was surrounded by a cold-shroud and the cryostat windows were covered to minimize the ambient radiation incident on the device. Figure 26 shows the dark noise from a 64 $\mu$ m diameter mesa device as a function of temperature. The values shown in the figure were measured at -2V bias. The dark noise drops rapidly with temperature down to about 225K and then starts to level out. Specific detectivity values as a function of wavelength were calculated from these noise

measurements and responsivity data. Figure 27 shows the  $D^*$  vs. wavelength data from the device at three different temperatures. The peak type-II detectivity ( $D^*$ ) at room temperature was  $3.8 \times 10^9 \text{ cm}\cdot\text{Hz}^{1/2}\cdot\text{W}^{-1}$ . Peak type-II detectivity ( $D^*$ ) at 200 K was  $5.6 \times 10^{10} \text{ cm}\cdot\text{Hz}^{1/2}\cdot\text{W}^{-1}$  at  $2.17 \mu\text{m}$ . Even though the responsivity decreases with temperature, the detectivity increases with temperature and is highest at 200K. This is because the reduction in dark noise with temperature more than offsets the loss in responsivity, and thus leads to increased detectivity.

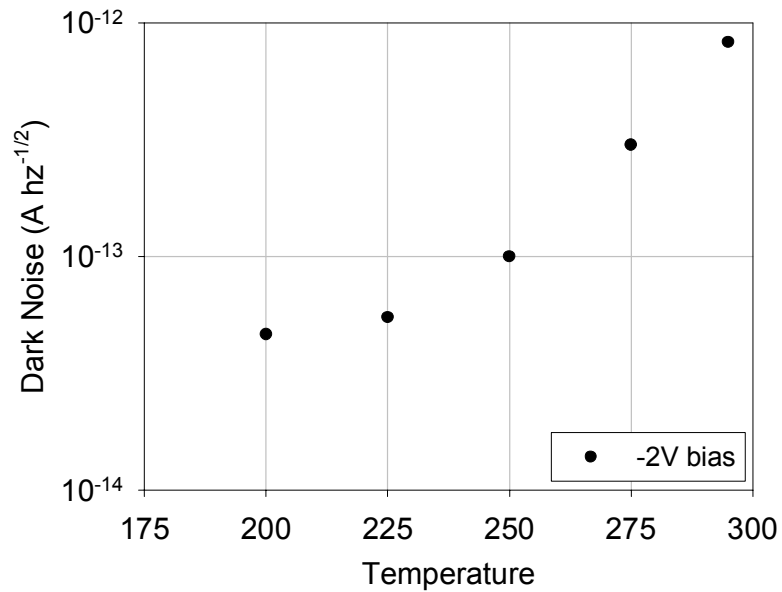


Figure 26. Dark noise vs. temperature measured at -2V bias from a  $64\mu\text{m}$  diameter device.

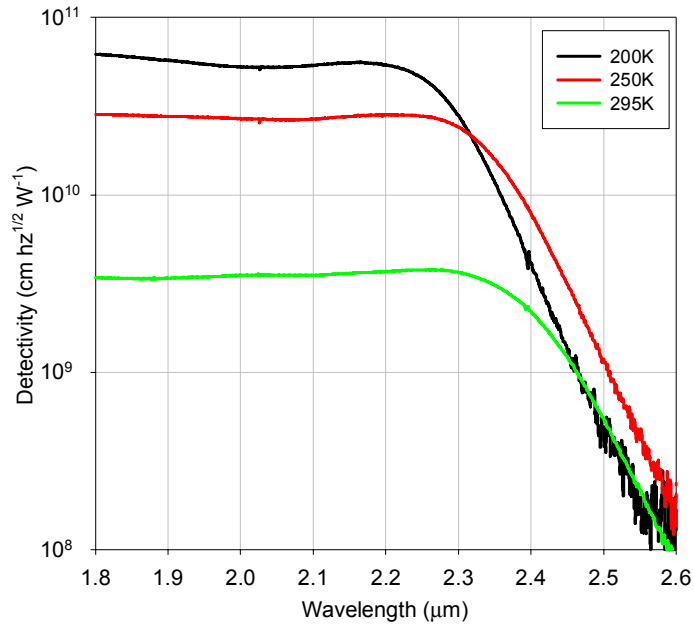


Figure 27. Specific detectivity at -2V as a function of wavelength, measured at different temperatures.

Many long wavelength p-i-n detectors are operated at zero bias. Devices operating in the photovoltaic mode often show higher detectivity because of greatly reduced dark current and dark noise. The reduction in dark-noise offset the loss in responsivity by going to lower bias. The other advantage is that the device consumes no power and does not require a power supply. Preliminary data from zero-bias measurements from these p-i-n devices suggests that detectivity values higher than  $1 \times 10^{11} \text{ cm} \cdot \text{Hz}^{1/2} \cdot \text{W}^{-1}$  may be possible at low temperatures. The dark-noise measured from the devices was below the noise floor of the low-noise current pre-amplifier (5 fA) at its highest gain setting ( $10^{-9} \text{ A/V}$ ).

As stated earlier, this device had a coating of 2000 Å of SiO<sub>2</sub> on the top surface, which results in approximately 20% back reflection of 2µm to 2.5µm wavelength incident light. In order to get increased coupling of incident light, an additional 1800 Å of SiO<sub>2</sub> were deposited as anti-reflection (AR) coating on the top. Since the mask layer to isolate the mesa tops for selective deposition of additional silicon dioxide was not available, additional silicon dioxide was deposited everywhere on one of the small processed pieces. The p- and n-contacts were opened again using photolithography. Calculated theoretical reflectivity from the top surface with 3800 Å of SiO<sub>2</sub> is approximately 0.05 at 2.3µm wavelength. This improved AR-coating led to peak external quantum efficiency of 43% at 2.23µm. The room temperature external quantum efficiency vs. wavelength curves are shown in Figure 28. Improved AR-coating led to an increase of about 22% in the measured external quantum efficiency.

A commensurate increase in the detectivity values is expected for devices with the improved AR-coating. However, during the deposition of the additional silicon dioxide, the passivation quality deteriorated, possibly because of prolonged heating and additional processing steps. This led to increased dark current and dark-noise from the devices with the AR coating. Therefore, the increased detectivity was not realized. It is possible to fabricate these devices such that they have a high quality surface passivation in addition to a high quality AR coating. High quantum efficiency and detectivity numbers can be expected from such devices.

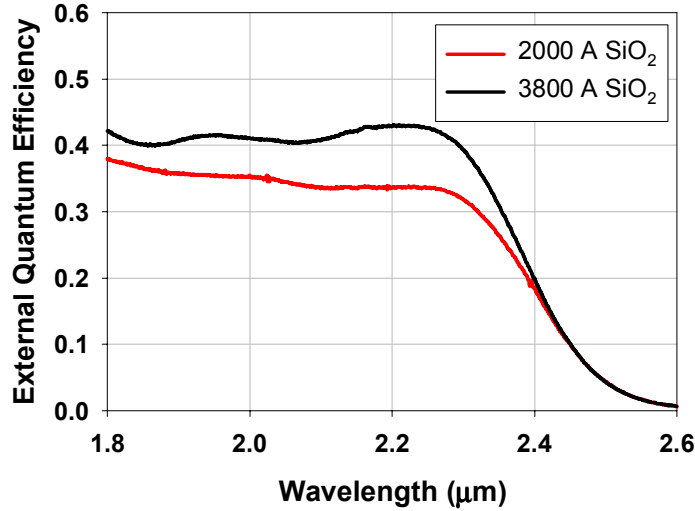


Figure 28. Room temperature external quantum efficiency as a function of wavelength from devices with two different top surface coatings. The external quantum efficiencies were measured at -2V bias.

## 5.5 SUMMARY

We have fabricated p-i-n photodiodes with 150 pairs of GaInAs-GaAsSb type-II quantum wells in the intrinsic-region. The structure was grown lattice-matched to InP substrate by molecular beam epitaxy. The devices exhibited low dark current and had a cutoff wavelength of 2.4μm. The room temperature low-bias dark current density was 5mA/cm<sup>2</sup>. Peak room temperature external quantum efficiency was measured to be 43% at 2.23μm, and the peak detectivity was 5.6x10<sup>10</sup> cm·Hz<sup>1/2</sup>·W<sup>-1</sup> at 200K. Better performance is expected from these devices under zero-bias operation. Further improvements in quantum efficiency and detectivity are possible by using an improved passivation with a better anti-



reflection coating. These devices showed high performance at temperatures well within the TE cooler range.

## **Chapter 6 Avalanche Photodiodes with GaInAs-GaAsSb type-II QWs**

### **6.1 INTRODUCTION**

In chapter 5, we discussed the results from p-i-n photodiodes with GaInAs-GaAsSb type-II quantum wells in the intrinsic region. In theory, it is possible to apply a high voltage across the intrinsic region of p-i-n devices to cause impact-ionization. This impact-ionization leads to avalanche gain, as discussed in chapter 4. However, the p-i-n devices discussed in the last chapter suffered from high tunneling current at high reverse bias, resulting in the photocurrent and dark current being almost identical. Therefore, no avalanche gain could be seen.

The tunneling current depends on the bandgap of the layers and the electric field in the layers, as shown in equation 4.5. In order to reduce the tunneling current, it is important to limit the electric field in the low bandgap regions. At the same time, a high electric field is required for significant gain. To meet both these criteria, the absorption and multiplication regions must be separated. In the separate absorption, charge, and multiplication (SACM) structure, the low bandgap absorption region is separated from the large bandgap multiplication region by a thin, lightly doped, field-control charge region [49]. This allows high electric field in the wide bandgap multiplication region causing avalanche multiplication; at the same time maintaining low electric field in the narrow bandgap layers to avoid tunneling.

## 6.2 THE SACM DEVICE STRUCTURE

The avalanche photodiode structure was designed to demonstrate high volume manufacturability. Two separate structures were grown with identical absorption regions. The first structure was designed to be processed into planar devices [58-60]. In this structure, a 4 $\mu\text{m}$  thick InP layer was grown on the top of the absorption and charge regions. This layer is meant to be separated into multiplication and p-contact layers through dopant diffusion. Collaborative work on this project is underway at Princeton Lightwave Inc., New Jersey.

The second structure with similar absorption and charge regions was designed to be processed into mesa devices. Since InP has a higher hole ionization coefficient ( $\beta$ ) than the electron ionization coefficient ( $\alpha$ ), we designed the APD as a hole-injection device. The schematic diagram of the SACM APD and the electric field profile is shown in Figure 29. The blue curve shows the electric field at punch-thru voltage, when the depletion region is at the edge of the absorption region. The red line shows the electric-field profile when there is high field in the multiplication region and low field in the absorption region. The growth sequence from the substrate up is described below.

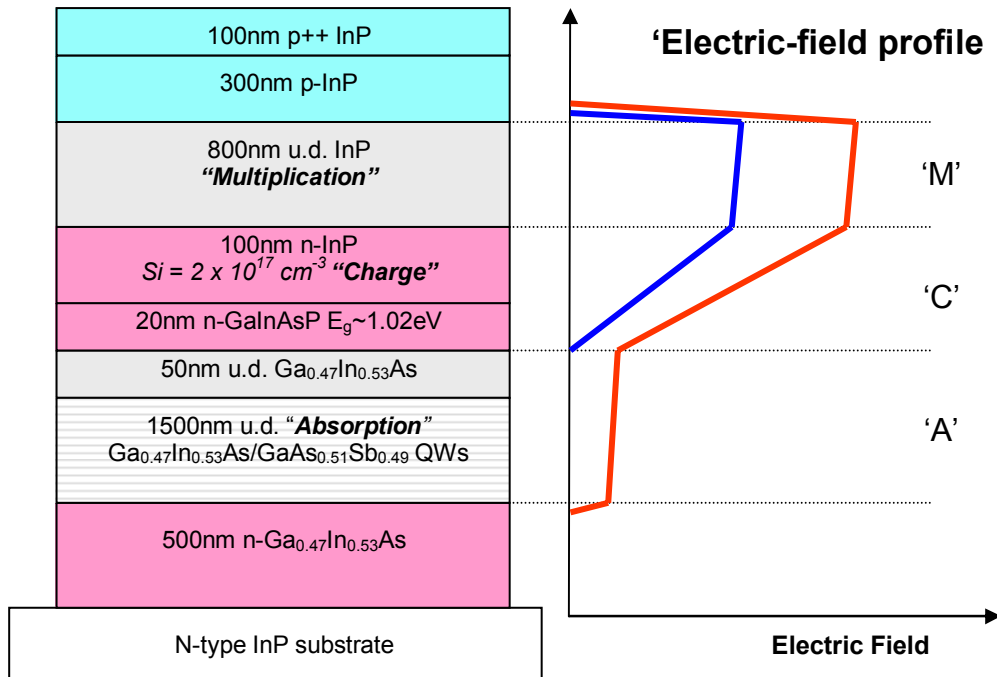


Figure 29. Schematic of the SACM avalanche photodiode structure and the electric- field distribution in the device at two different reverse bias voltages.

A 500nm thick n-type doped ( $\text{Si}: 3 \times 10^{18} \text{ cm}^{-3}$ )  $\text{Ga}_{0.47}\text{In}_{0.53}\text{As}$  layer was first grown to serve as a buffer layer and the n-contact layer. The absorption region was grown next, and consisted of 150 pairs of un-doped  $\text{Ga}_{0.47}\text{In}_{0.53}\text{As}$ - $\text{GaAs}_{0.51}\text{Sb}_{0.49}$  type-II quantum wells. Each layer in the absorption region was 5nm thick. Following the absorption region, a lightly n-type doped ( $\text{Si}: 2 \times 10^{17} \text{ cm}^{-3}$ ) charge region was grown. This region consisted of a 20nm thick  $\text{GaInAsP}$  ( $E_g = 1.02\text{eV}$ ) and a 100nm thick  $\text{InP}$  layer. Next, an 800nm thick un-doped  $\text{InP}$  layer was grown as the multiplication region. On top of the multiplication region, a 300nm thick p-type doped ( $\text{Be}: 3 \times 10^{18} \text{ cm}^{-3}$ )  $\text{Ga}_{0.47}\text{In}_{0.53}\text{As}$  layer was grown.

Finally a 100nm thick, highly p-type doped (Be:  $3 \times 10^{19} \text{ cm}^{-3}$ )  $\text{Ga}_{0.47}\text{In}_{0.53}\text{As}$  layer formed the p-contact layer.

Since there is a large barrier for holes transiting from the GaInAs-GaAsSb absorption region to the InP multiplication region, the  $\text{Ga}_{0.47}\text{In}_{0.53}\text{As}$  -GaInAsP-InP sequence of layers provides a graded step to avoid hole-trapping at the hetero-interface [26, 61].

### **6.3 GROWTH AND FABRICATION**

The device structure was grown on n-type (001) InP substrate supplied by American Xtal Technologies. Prior to epitaxial growth, the substrate surface was prepared as explained in section 5.3. The first  $2\mu\text{m}$  of the structure were grown at  $525^\circ\text{C}$ . Ten second interrupts were used between the growth of  $\text{Ga}_{0.47}\text{In}_{0.53}\text{As}$  and  $\text{GaAs}_{0.51}\text{Sb}_{0.49}$  layers. During the growth of the  $\text{Ga}_{0.47}\text{In}_{0.53}\text{As}$  layer between the absorption region and the charge region, the growth temperature was ramped down to  $480^\circ\text{C}$ . The rest of the structure was grown at this temperature since InP layers grow better at lower temperature [46].

### **6.4 DEVICE RESULTS**

The grown structure was processed into top illuminated mesa devices of various sizes, as discussed in Chapter 3. The results of electrical measurements from these devices are presented below.

### 6.4.1 DC characteristics and avalanche gain

Reverse current-voltage characteristics of the avalanche photodiodes were measured using an Agilent 4156B semiconductor parameter analyzer. The dark current measured from different size devices showed a quadratic dependence on the device diameter. This suggests that most of the dark current is generated in the bulk of the devices and there is little contribution from surface leakage. Figure 30 shows the reverse current-voltage data at different temperatures measured from a 36 $\mu\text{m}$  diameter mesa device. The punchthrough voltage at room temperature is about -37V and the device breakdown is at  $\sim$  -52V. Room temperature dark current at punchthrough voltage is 72nA. At 90% of breakdown voltage, the room temperature dark current is 198nA. The dark current drops rapidly with temperature, and at 225K, the dark current at 90% of breakdown is 1.4nA, corresponding to current density of 138 $\mu\text{A}/\text{cm}^2$ .

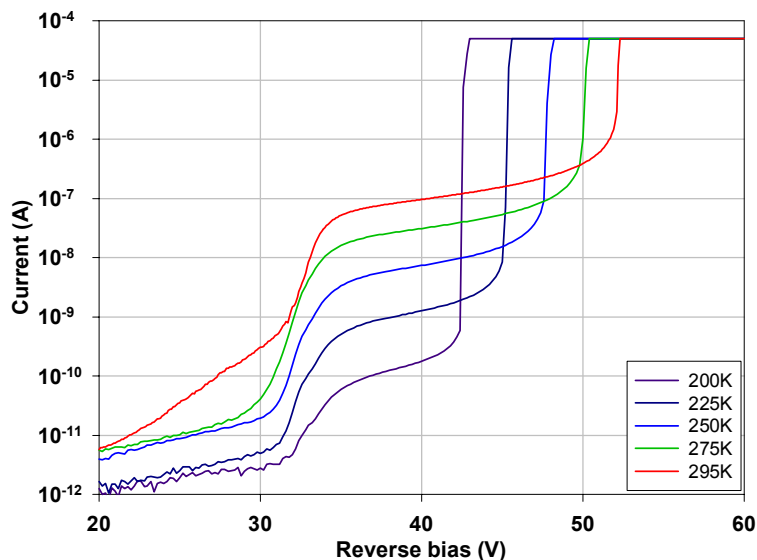


Figure 30. Reverse I-V data at different temperatures.

The dark current values at punchthrough are similar to the dark current from the p-i-n photodiodes at low bias. The primary mechanism contributing to dark current at low electric fields is the thermal generation of carriers. At high bias voltages close to breakdown, the electric field in the absorption region is not high enough to cause tunneling. The avalanche breakdown occurs at lower voltages at reduced temperatures because of decreased phonon scattering at low temperatures. The breakdown voltage drops at a rate of about 110mV/K.

Photocurrent and dark current data from a 44 $\mu$ m-diameter device at room temperature and 225K are plotted in Figure 31 (a) and (b), respectively. It can be seen from the slope of the photo-response that there is avalanche gain at punchthrough. This gain at punchthrough was determined by comparing the photocurrent from a 64 $\mu$ m diameter APD biased at -37V to the photocurrent of a p-i-n device of the same size, under the same illumination from a 1.55 $\mu$ m wavelength laser. The laser light was focused to a 10 $\mu$ m-diameter spot on the devices. The p-i-n photodiode had the same absorption region, and was biased at low voltage to insure unity gain. The ratio of the photocurrents at room temperature was 1.7, which was assumed to be the room-temperature gain of the APD at -37V. Multiplication gain at a given electric field has temperature dependence because of the change in electron and hole ionization coefficients with temperature. The gain at 225K was determined by comparing the responsivity of the APD at that temperature to the responsivity of the p-i-n device measured at the same temperature. The responsivity values at 2.2 $\mu$ m were used to calculate the low temperature gain. Even though the two photodiodes had similar

absorption regions, their responsivity curves have slightly different shapes. Thus some error is introduced in the determination of gain by this method. The gain curves as a function of bias voltage are also plotted in Figure 31.

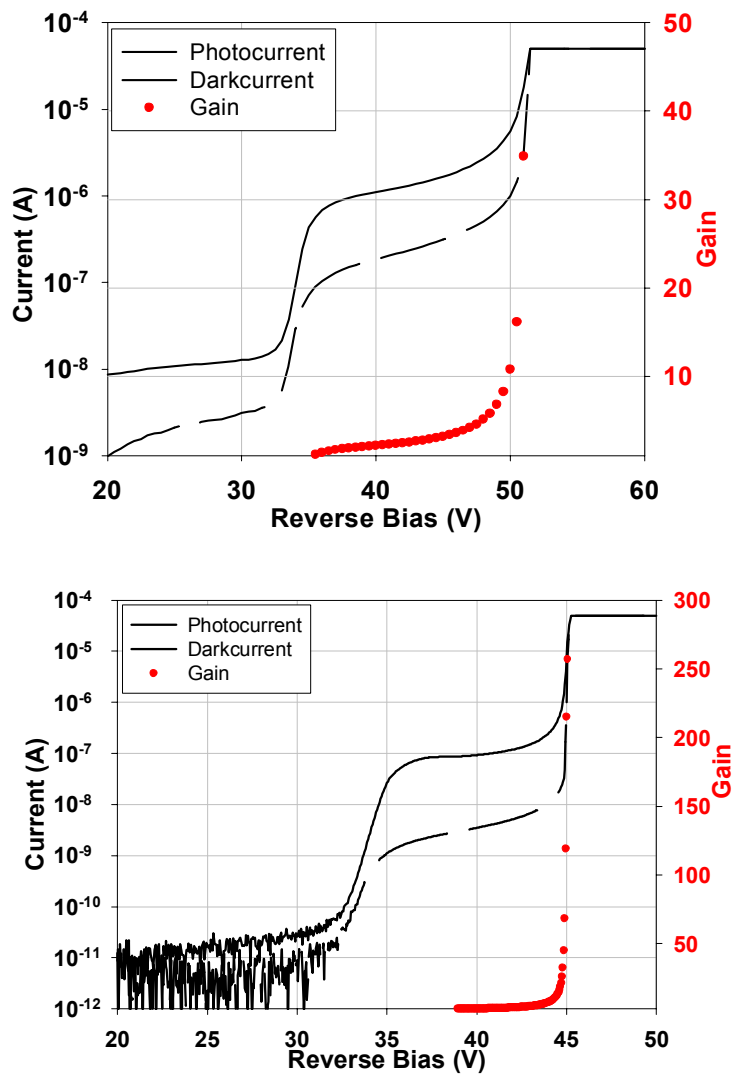


Figure 31. Photocurrent (solid line), dark current (dashed lines) and avalanche gain (red circles) at room-temperature (top) and 225 K (bottom).



### 6.4.2 Optical response

A Nicolet Magna-II FTIR spectrometer with a SRS 570 low-noise current preamplifier was used to measure the spectral response at different temperatures and bias conditions. The SRS 570 preamplifier is equipped to provide up to  $\pm 5V$  of dc bias to the photodiode. In the case of the p-i-n photodiodes, this adjustable dc voltage was used to bias the devices. However, to measuring the APD spectral response, a much higher dc bias is required. A set of 9V batteries were placed in series with the APD and the preamplifier input, as shown in Figure 32(a). Figure 32(b) shows the equivalent biasing circuit. The batteries were set up to provide 45V reverse bias to the APD under test. The adjustable dc bias from the preamplifier was used to tune the bias voltage across the APD. The same biasing scheme was used in measuring the blackbody responsivity and dark noise of the device.

The normal incidence photo-response spectra measured at various temperatures at -37V reverse bias are shown in Figure 33. The measured data at each temperature was normalized to the peak value at that temperature. These peak values were from the type-I (spatially direct) peaks from  $Ga_{0.47}In_{0.53}As$  and  $GaAs_{0.51}Sb_{0.49}$  QWs at about  $1.5\mu m$  (not shown in the figure.) The type-II (spatially indirect) response from  $1.8\mu m$  to  $2.5\mu m$  is shown in the figure. The photo-response data from the FTIR was calibrated using a PbS detector with known responsivity, and was verified using a second calibrated long-wavelength GaInAs detector. As expected, the photo-response red-shifts with increase in temperature, because of the reduction of the bandgaps at higher temperature.

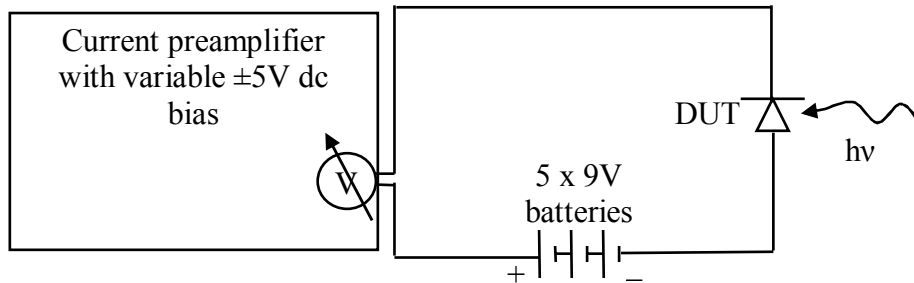
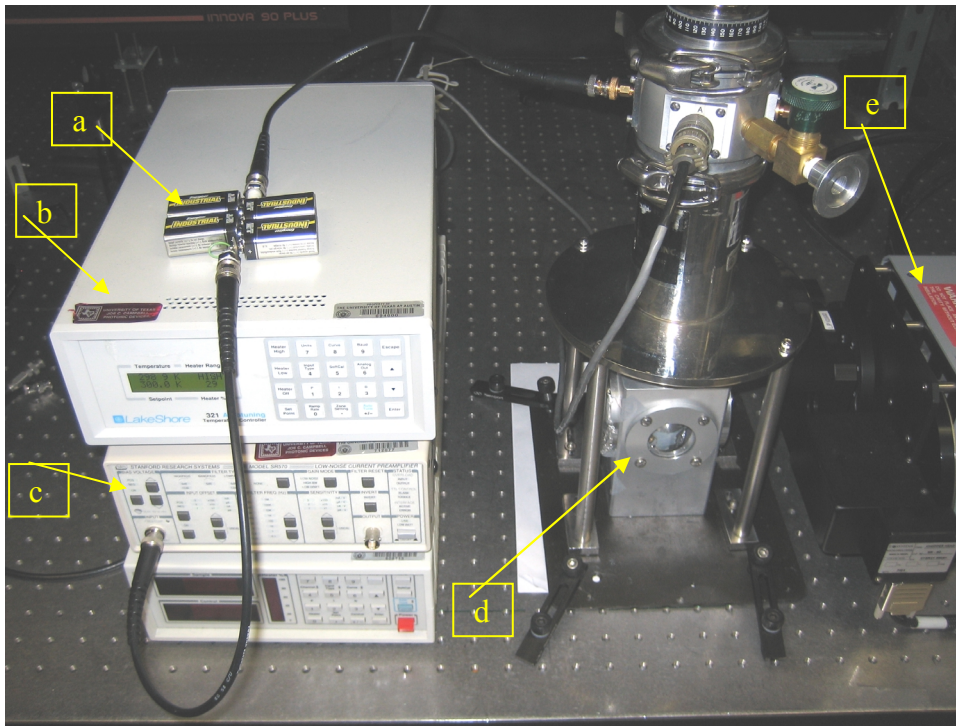


Figure 32. (a) The APD responsivity measurement apparatus and (b) the equivalent biasing circuit using 9V batteries. a: 9V batteries in series with the photodiode and the pre-amplifier input; b: temperature controller; c: SRS 570 pre-amplifier; d: cryostat with the device inside; e: blackbody source.

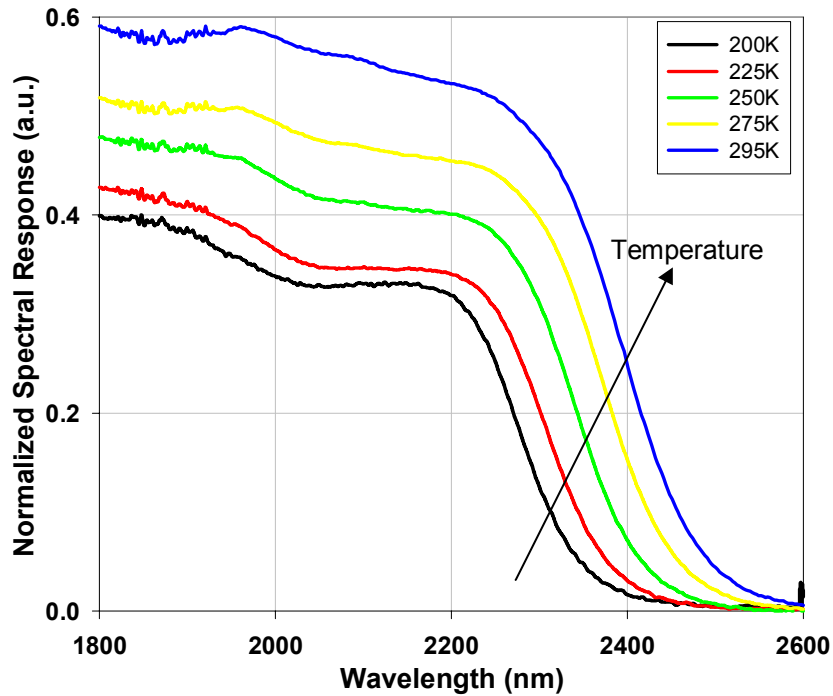


Figure 33. Photo-response of the APD at different temperatures, measured at -37V bias.

The relative response (and responsivity) increases with temperature. We believe that this is due to photo-generated carriers having more energy to escape the QWs and transit to the electrodes. Room temperature spectral response measured at different reverse bias voltages is shown in Figure 34. The shape of the spectral response changes with bias voltage. Further investigation is required to understand the relation between electric field across the absorption region and the shape of the optical-response.

Responsivity of this device was measured as described in Sections 4.5.1 and 5.4.3. Room temperature responsivity of the device at -37V is shown in Figure 35. The diagonal lines in the graph represent equivalent *unity gain* external

quantum efficiency. The calculated quantum efficiency at -37V was divided by 1.7 (room temperature gain at punchthrough) to get the unity gain quantum efficiency.

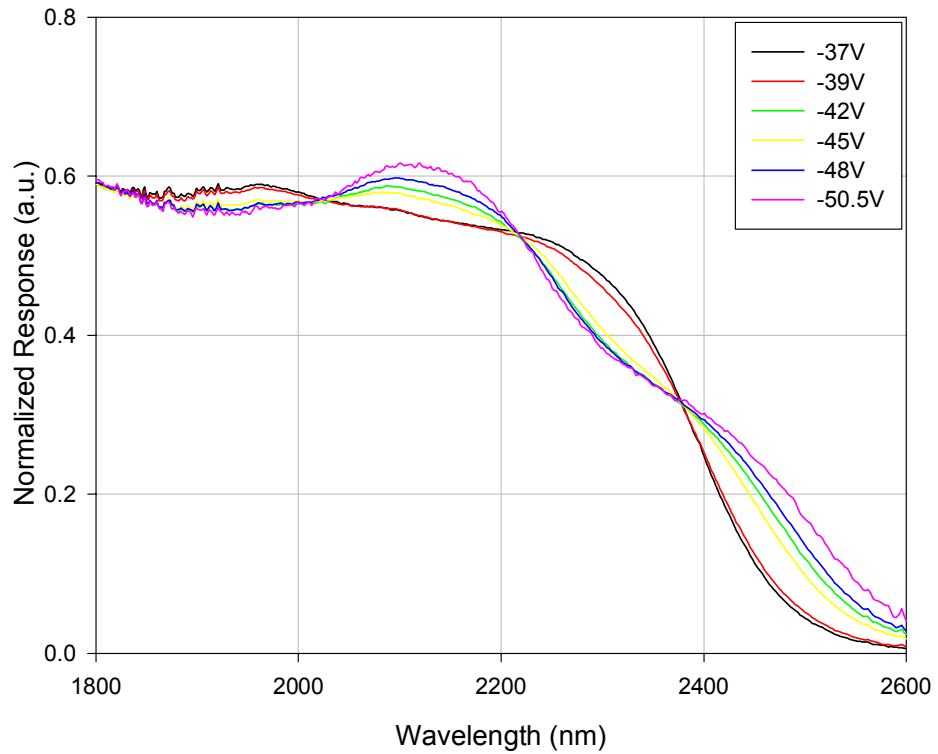


Figure 34. Room-temperature spectral response of the APD at different reverse-bias voltages.

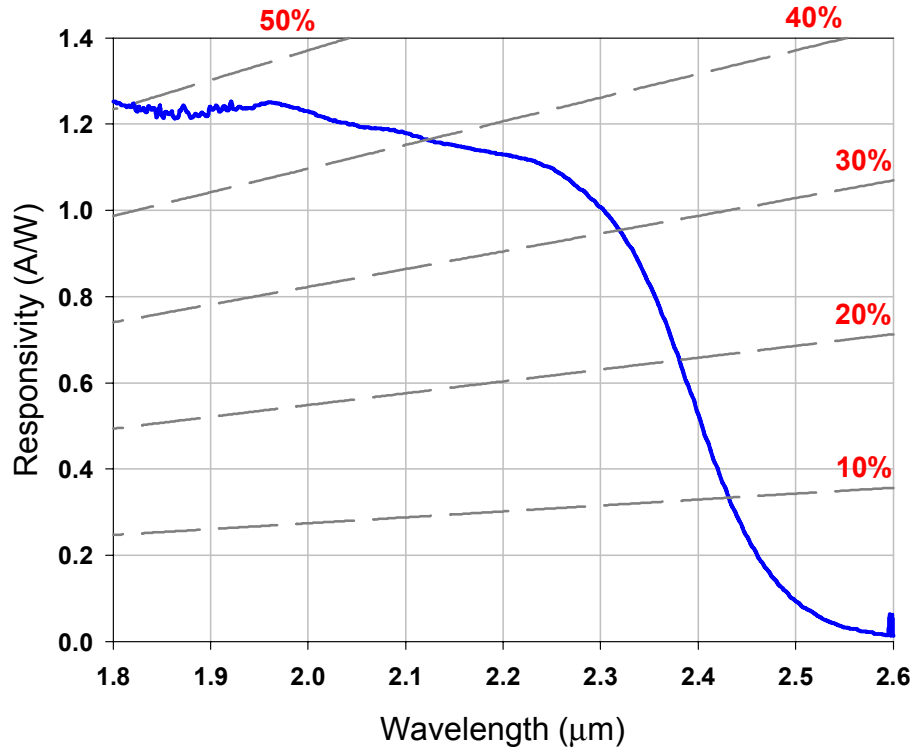


Figure 35. Room-temperature responsivity vs. wavelength of the APD at -37V bias. The equivalent external quantum efficiency is represented by the grey (dashed) lines and numbers in red.

### 6.4.3 Noise and detectivity

Figure 36 shows the noise current from the device at different reverse bias voltages, at two different temperatures. The data is plotted on a semi-log plot. The low temperature noise current has a complicated dependence on the bias voltage. This dependence comes from the scaling of gain with voltage, and the scaling of noise current with gain. The former can be approximated to an exponential dependence and the latter is explained in equation 4.14. At higher temperature, the noise current is most likely dominated by the thermally generated carriers. Therefore the effect of voltage is negligible. It must be kept in mind that the avalanche gain values are different at different temperatures for the same reverse bias.

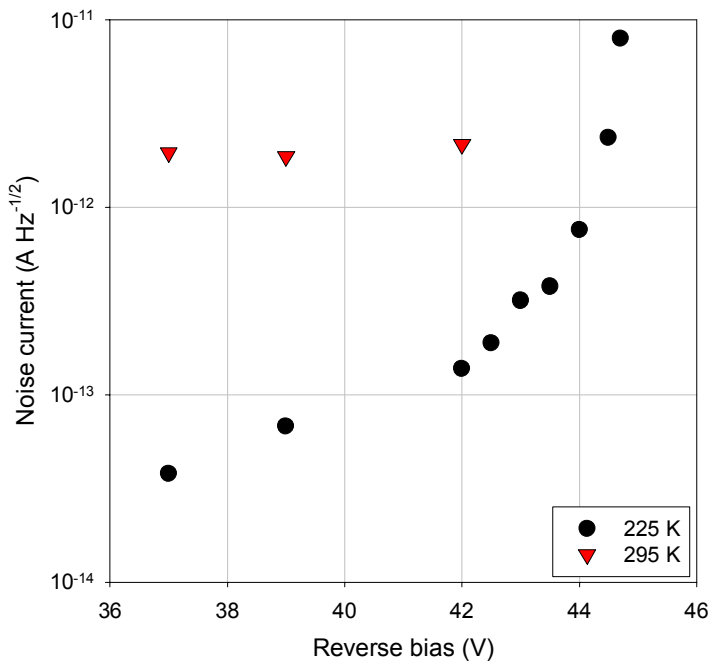


Figure 36. Noise-current from the APD vs. reverse bias voltage, measured at 225K (black circles) and room-temperature (red triangles).

Figure 37 shows the noise current at punchthrough voltage at different temperatures. Even though the gain at punchthrough changes with temperature, all the gain values are small. Therefore the noise current increases exponentially with temperature, as expected from equation 4.4.

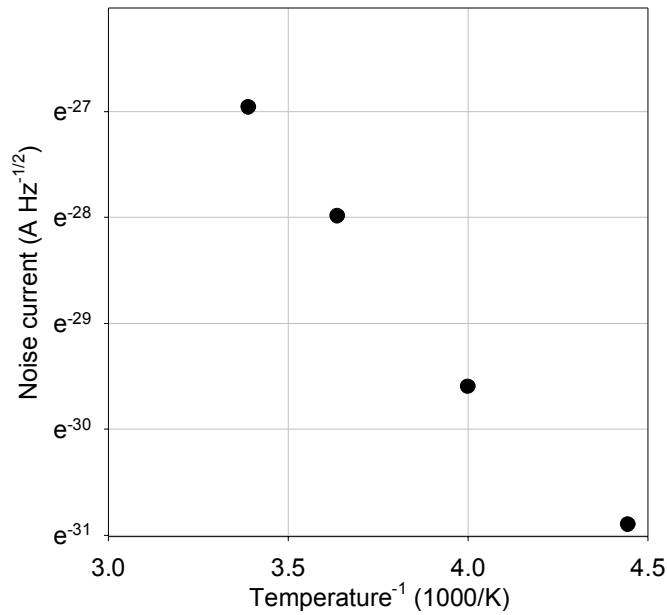


Figure 37. APD noise-current vs. temperature, measured at punchthrough (-37V).

The detectivity versus wavelength data for different bias voltages and temperatures is shown in Figure 38(a) and (b). Even though the responsivity increases with gain, the detectivity values drop at high bias because of increased noise current. A thin multiplication region with low avalanche noise is expected to improve the high gain detectivity of these avalanche photodiodes [54-56].

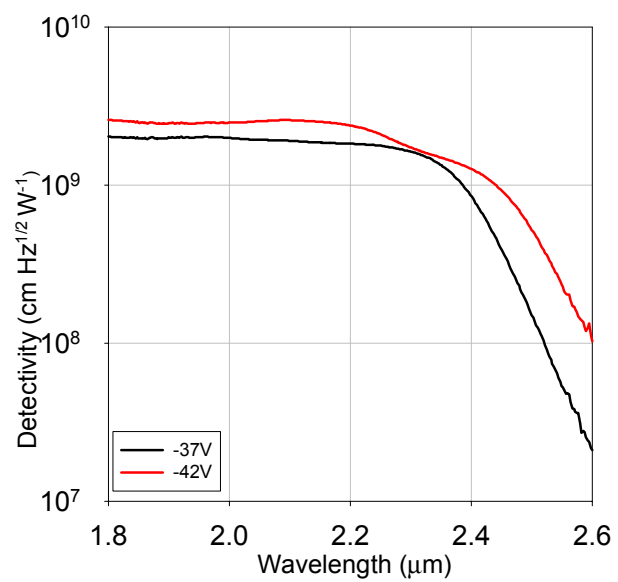
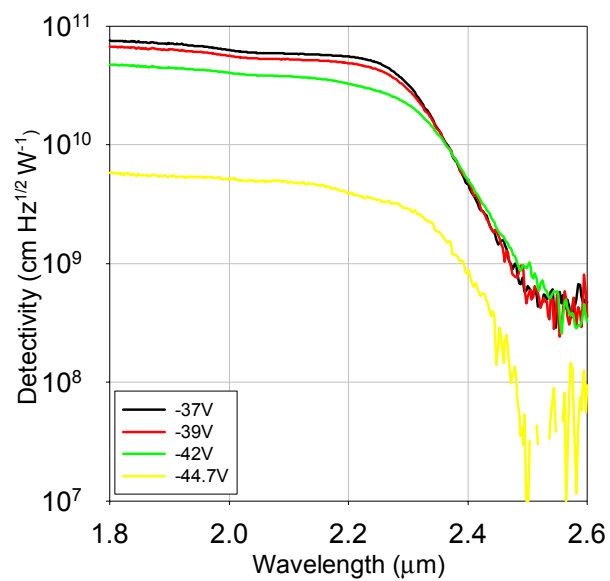


Figure 38. Detectivity vs. wavelength at different reverse bias voltages, measured at 225K (top) and room temperature (bottom).



## 6.5 SUMMARY

We have demonstrated InP based avalanche photodiodes with response up to 2.4 $\mu\text{m}$ , using  $\text{Ga}_{0.47}\text{In}_{0.53}\text{As-GaAs}_{0.51}\text{Sb}_{0.49}$  type-II quantum wells. The hole-injection, separate absorption, charge, and multiplication structure was grown lattice- matched to the InP substrate. The devices achieved room temperature gain in excess of 30 and had type-II room temperature external quantum efficiency of 38% at 2.2  $\mu\text{m}$ . At 225K, the devices exhibited gain in excess of 250 and dark current density of 138 $\mu\text{A}/\text{cm}^2$  close to breakdown.

## Chapter 7 Conclusions and Future Work

### 7.1 CONCLUSIONS

Indium Phosphide based photodiodes using GaInAs/GaAsSb type-II quantum wells (QWs) for mid-wave infrared (MWIR) detection are promising alternatives to mercury-cadmium-tellurium based devices. The mature InP device and materials technologies can lead to high uniformity and high performance MWIR photodiodes for near room-temperature operation. This dissertation discussed the fabrication and performance of InP based p-i-n and avalanche photodiodes with room-temperature cutoff wavelengths of 2.4 $\mu$ m.

Good quality crystal growth of GaAsSb on InP involves accurate understanding of the effect of the growth parameters on the crystal composition and quality. We found that increasing the growth temperature or decreasing the group-III growth rate leads to reduced Sb incorporation in the film. We also determined that As incorporates preferentially over Sb. The effect of As and Sb beam equivalent pressures (BEPs) on the layer composition was studied. Optimal growth temperature for GaAs<sub>0.51</sub>Sb<sub>0.49</sub> on InP was found to be about 525°C with both As and Sb BEPs of 3.0x10<sup>-6</sup> torr.

The Ga<sub>0.47</sub>In<sub>0.53</sub>As- GaAs<sub>0.51</sub>Sb<sub>0.49</sub> type-II QWs were grown as the intrinsic region of a p-i-n device to demonstrate long wavelength absorption. The devices exhibited low dark current and had a room temperature external quantum efficiency of 43% at 2.23 $\mu$ m. The low bias dark current density at room

temperature was less than  $5\text{mA}/\text{cm}^2$ . Peak type-II detectivity ( $D^*$ ) at 200 K was  $5.6 \times 10^{10} \text{ cm } \sqrt{\text{Hz}} \text{ W}^{-1}$  at  $2.17 \mu\text{m}$ .

A similar absorption region consisting of 150 pairs of  $\text{Ga}_{0.47}\text{In}_{0.53}\text{As}$ - $\text{GaAs}_{0.51}\text{Sb}_{0.49}$  type-II QWs was incorporated in a separate absorption, charge, and multiplication (SACM) avalanche photodiode (APD) structure. The APDs exhibited room temperature gains above 30 and 225K gains of above 250. The 225K dark current density at 90% of breakdown voltage was  $138\mu\text{A}/\text{cm}^2$ .

Even though the high avalanche gains in the APDs led to high responsivity values, the noise associated with the avalanche multiplication degraded the device detectivities. The p-i-n photodiodes, on the other side, had very low noise at zero bias operation. Even though they have lower responsivity at zero bias, the reduced noise is expected to result in much improved detectivity values. The above comparison seems to suggest that the avalanche photodiodes are disadvantageous in detecting low intensity signals. However, from a systems perspective, the amplifiers used downstream from the photodiodes add noise to the electrical signal and are often the limiting factor in the system sensitivity. Therefore, avalanche photodiodes operated at moderate gains may actually result in higher system sensitivity, as long as the avalanche noise is less than the amplifier noise.

## **7.2 FUTURE WORK**

The photodiodes discussed in this dissertation are the first set of devices made to explore the possibility of fabricating MWIR detectors on InP. The results we obtained are very encouraging. Furthermore, there is much room for

improvement in device performance. Some of the recommended future work is discussed below:

- [1] Optimize the crystal quality: The quality of GaInAs, GaAsSb and the interfaces between these layers is directly tied to the dark current generation through trap levels. Improvements in the crystal and interface quality can lead to greatly reduced dark current values and in turn lead to much improved detectivity at higher temperatures. The growth temperature and the group-V BEPs for GaAsSb growth can be further optimized. The interrupt times and the group-V fluxes used at the interfaces also need to be optimized to obtain abrupt defect free interfaces.
- [2] Incorporate low noise multiplication regions: The multiplication noise of an avalanche photodiode can be reduced by going to thinner multiplication regions and/or using a material with a low 'k' value. Impact ionization engineered multiplication regions can further lower the multiplication noise of the APDS, thereby improving the high-gain detectivity [54-56, 62]. An electron injection APD with a thin AlInAs multiplication region will have lower avalanche noise.
- [3] Using strain-compensation in QWs: Our initial calculations of band-offsets between different compositions of GaInAs and GaAsSb have shown that the effective type-II bandgap decreases for certain moderately strained compositions. The principle of strain compensation, where the tensile strain in one layer is compensated by compressive strain in another layer, can be used to engineer the bandgap to absorb wavelengths up to

about 5 $\mu\text{m}$ . The widths of the quantum wells determine the energy of the confined states within the wells. Thus the QW thickness can be used as another wavelength tuning parameter, in addition to the layer compositions.

[4] Improve quantum efficiency: The total number of lattice matched or strain-compensated type-II QWs can be increased to enhance the quantum efficiency of the photodiodes. Additionally, a distributed Bragg reflector (DBR) mirror (AlAsSb/GaInAs) can be epitaxially grown under the device to effectively double the absorption length of the photodiode.

There is an apparent point of diminishing returns in trying to increase the detectivity by simply increasing the number of QWs. The dark current generated in the narrow bandgap layers and in the interfaces will eventually lead to high dark noise and reduced detectivity. Thick device structures also result in slow speeds and high breakdown voltages. Two alternatives are the resonant-cavity structure and the waveguide structure. In a resonant-cavity enhanced (RCE) structure, the device is sandwiched between two DBR mirrors. Very high quantum efficiencies can be obtained with thin absorption regions [63]. The disadvantages of this structure are the relatively complicated material growth and processing and a narrow wavelength response. The waveguide structures can also achieve high quantum efficiencies from thin absorption regions, but coupling the incident light to these devices can be challenging [64].

## Appendix A

### Blackbody Responsivity Calculations

#### I. Defining Constants

$$\mu := 10^{-6}$$

$$\mu\text{m} := 10^{-6} \cdot \text{m}$$

$$n := 10^{-9}$$

$$c := 2.998 \cdot 10^{10} \cdot \text{cm} \cdot \text{s}^{-1}$$

$$k := 1.381 \cdot 10^{-23} \cdot \text{J} \cdot \text{K}^{-1}$$

$$\sigma := 5.67 \cdot 10^{-12} \cdot \text{W} \cdot \text{cm}^{-2} \cdot \text{K}^{-4}$$

$$q := 1.6 \cdot 10^{-19} \cdot \text{C}$$

$$h := 6.626 \cdot 10^{-34} \cdot \text{J} \cdot \text{s}$$

Window transmission

$$T_{\text{ZnSe}} := 0.92$$

Room Temp., also chopper temperature

$$T_1 := 295 \cdot \text{K}$$

Black body temperature

$$T_2 := (273.15 + 900) \cdot \text{K}$$

#### II. Photon flux per unit area from blackbodies

Photon flux per unit area, spectral interval for blackbodies

Planck's radiation law

$$N(\lambda, T) := \frac{2 \cdot \pi \cdot h \cdot c^2}{\lambda^5} \cdot \frac{1}{\frac{h \cdot c}{k \cdot T \cdot \lambda} - 1}$$

The photon flux per unit area from blackbody (at  $T_2$  K), less radiation from chopper (at  $T_1$  K)

$$M(\lambda_1, \lambda_2) := \int_{\lambda_1}^{\lambda_2} N(\lambda, T_2) d\lambda - \int_{\lambda_1}^{\lambda_2} N(\lambda, T_1) d\lambda$$

$$M1(\lambda) := N(\lambda, T_2) - N(\lambda, T_1)$$

### III. Photon flux on samples

distance from the blackbody aperture to detector

$$d := 9.3 \text{ in}$$

blackbody aperture diameter

$$D_{\text{ap}} := 15.9 \text{ mm}$$

device mesa diameter

$$d_s := 156 \mu\text{m}$$

top contact diameter

$$d_c := 40 \mu\text{m}$$

device area for incident light

$$A_{\text{det}} := \frac{\pi}{4} \cdot (d_s^2 - d_c^2)$$

Incident power on device:

$$P_{\text{inc}}(\lambda_1, \lambda_2) := M(\lambda_1, \lambda_2) \cdot \frac{\frac{\pi}{4} \cdot D_{\text{ap}}^2}{\pi \cdot d^2} \cdot T_{\text{ZnSe}} \cdot 0.45 \cdot A_{\text{det}}$$

### IV. Blackbody Responsivity

Preamplifier gain

$$G := 500 \text{ n} \cdot \frac{\text{A}}{\text{V}}$$

FFT spectrum analyzer reading (total responsivity current)

$$V_{\text{rms}} := 193.2 \text{ mV}$$

Signal current

$$I_{\text{sig}} := V_{\text{rms}} \cdot G$$

Reading Data from file:

Col 0 = wavelength (microns)

Col 1 = LP1800 filter transmission

Col 2 = relative response from FTIR (a.u.)

Q :=



Writing data into another variable:

index variable

$$i := 1..731$$

wavelength (um)

$$\text{DATA}_{i,1} := Q_{i,0}$$

filter transmission

$$T_{f,i,1} := Q_{i,1}$$

FTIR response (a.u.)

$$\text{DATA}_{i,2} := Q_{i,5}$$

wavelength step (um)

$$\text{DATA}_{i,3} := Q_{i,0} - Q_{i+1,0}$$

Blackbody radiation as a function of wavelength, reduced to a.u.

$$\text{DATA}_{i,4} := M1(\text{DATA}_{i,1} \cdot \mu\text{m}) \cdot \frac{\text{m}^3}{\text{W}}$$

Product of FTIR response, BB radiation and %T of LP1800



$$\text{DATA}_{i,5} := \text{DATA}_{i,2} \cdot \text{DATA}_{i,4} \cdot \frac{T_{f,1}}{100}$$

Area under the FTIR \* BB radiation \* %T --λ curve

$$\text{sum}_1 := \sum_{i=1}^{731} (\text{DATA}_{i,5} \cdot \text{DATA}_{i,3})$$

Relative Response

$$\text{DATA}_{i,6} := \frac{\text{DATA}_{i,5} \cdot \text{DATA}_{i,3}}{\text{sum}_1}$$

Sum of all relative responses should be = 1.0

Responsivity calculation:

$$\text{Resp}_i := \frac{I_{\text{sig}} \cdot \text{DATA}_{i,6}}{\left[ M \left[ \text{DATA}_{i,1} \cdot \mu\text{m}, (\text{DATA}_{i,1} + \text{DATA}_{i,3}) \cdot \mu\text{m} \right] \cdot \left( \frac{D_{\text{ap}}}{2 \cdot d} \right)^2 \cdot T_{\text{ZnSe}} \cdot \frac{T_{f,1}}{100} \cdot 0.707 \cdot A_{\text{det}} \right]}$$

EQE is Responsivity x 1.24 / wavelength (um)

$$\text{EQE}_i := \frac{\text{Resp}_i \cdot 1.24}{\text{DATA}_{i,1}} \cdot \frac{\text{W}}{\text{A}}$$

Detectivity is Responsivity x sqrt(area)/noise current

$$\text{Det} := \frac{\text{Resp} \cdot \sqrt{A_{\text{det}}}}{6.5 \cdot \mu \cdot V \cdot \sqrt{s} \cdot 500 \text{ n} \cdot \frac{\text{A}}{\text{V}}}$$

## Bibliography

1. Michel, K., et al., *Monitoring of pollutant in waste water by infrared spectroscopy using chalcogenide glass optical fibers*. Sensors and Actuators B, 2004. **101**: p. 252-259.
2. Sandstrom, L., et al., *Gas monitoring using semiconductor lasers operating in the 2 $\mu$ m wavelength region*. Infrared Physics and Technology, 1998. **39**: p. 69-75.
3. Schiff, H.I., et al., *Some applications of NIR tunable diodes for remote sensing*. Physics and Technology, 1996. **37**: p. 39-43.
4. Fischer, C., et al., *Photoacoustic monitoring of gases using a novel laser source tunable around 2.5  $\mu$ m*. Optics and Lasers in Engineering, 2005. **43**(3-5): p. 573-582.
5. Palmer, J. and A.C. Davenhall, *The CCD Photometric Calibration Cookbook*. 2001: Starlink.
6. Carter, B.L., et al., *High detectivity GaInAsSb pin infrared photodetector for blood glucose sensing*. Electronics Letters, 2000. **36**(15): p. 1301-1303.
7. Olesberg, J.T., *Noninvasive blood glucose monitoring in the 2.0-2.5  $\mu$ m wavelength range*. 2001.
8. Bajaj, J. *HgCdTe infrared detectors and focal plane arrays*. 1998.
9. Caulfield, J.T., *Next generation IR focal plane arrays and applications*. 2003.
10. Gunapala, S.D., et al., *640 $\times$ 486 long-wavelength two-color GaAs/AlGaAs quantum well infrared photodetector (QWIP) focal plane array camera*. Electron Devices, IEEE Transactions on, 2000. **47**(5): p. 963-971.
11. Rogalski, A., *Assessment of HgCdTe photodiodes and quantum well infrared photoconductors for long wavelength focal plane arrays*. Infrared Physics and Technology, 1999. **40**: p. 279-294.
12. Vaidyanathan, M., et al., *High performance ladar focal plane arrays for 3D range imaging*. 2004.
13. Zandian, M., *Mid Wavelength Infrared p-on-n HgCdTe Heterostructure Detectors: 30-120 Kelvin State-of-The-Art Performance*. Journal of Electronic Materials, 2003. **32**(7): p. 803-809.
14. Phillips, J.D., et al., *Uniformity of optical absorption in HgCdTe epilayer measured by infrared spectromicroscopy*. Applied Physics Letters, 2003. **83**: p. 3701-3703.
15. Philips, J., et al., *Evaluation of the fundamental properties of quantum dot infrared detectors*. Journal of Applied Physics, 2002. **91**(7): p. 4590-4594.

16. Fuchs, F., et al., *InAs/GaInSb infrared superlattice photodiodes for infrared detection*. Proceedings of SPIE, 1998. **3287**: p. 14-21.
17. Fuchs, F., et al., *High performance InAs/Ga<sub>1-x</sub>In<sub>x</sub>Sb superlattice infrared photodiodes*. Applied Physics Letters, 1997. **71**(22): p. 3251-3253.
18. Vincent, J.D., *Fundamentals of Infrared Detector Operation and Testing*. 1990: John Wiley & Sons.
19. Rogalski, A., *Infrared detectors: an overview*. Infrared Physics & Technology, 2002. **43**(3-5): p. 187-210.
20. Rogalski, A., *Infrared detectors: status and trends*. Progress in Quantum Electronics, 2003. **27**(2-3): p. 59-210.
21. Norton, P., *HgCdTe infrared detectors*. Opto-electronics Review, 2002. **10**(3): p. 159-174.
22. Lyon, T.J.d., et al., *Epitaxial growth of HgCdTe 1.55- $\mu$ m avalanche photodiodes by molecular beam epitaxy* Proceedings of SPIE, 1999. **3629**: p. 256-267.
23. Hasnain, G., et al., *Mid-infrared detectors in the 3--5  $\mu$ m band using bound to continuum state absorption in InGaAs/InAlAs multiquantum well structures*. Applied Physics Letters, 1990. **56**(8): p. 770-772.
24. Levine, B.F., *Quantum-well infrared photodetectors*. Journal of applied physics, 1993. **74**(8): p. R1-R81.
25. Ye, Z., *Design, Fabrication and Characterization of Quantum Dot Infrared Photodetectors*. Electrical and Computer Engineering Department, The University of Texas at Austin 2003. **Ph.D.**
26. Vurgaftman, I., J.R. Meyer, and L.R. Ram-Mohan, *Band parameters for III-V compound semiconductors and their alloys*. Journal of Applied Physics, 2001. **89**(11): p. 5815-75.
27. Giehl, A.R., et al., *Waveguide-based type-II heterostructure photodiode on InAs substrate with broad wavelength range photoresponse*. Photonics Technology Letters, IEEE, 2004. **16**(5): p. 1358-1360.
28. Dries, J.C., et al., *A 2.0  $\mu$ m cutoff wavelength separate absorption, charge, and multiplication layer avalanche photodiode using strain-compensated InGaAs quantum wells*. 1999.
29. Dries, J.C., et al., *Strain compensated In<sub>1-x</sub>Ga<sub>x</sub>As (x<0.47) quantum well photodiodes for extended wavelength operation*. 1998.
30. Umezawa, T., et al., *Low dark current InGaAs p-i-n photodiodes with wide sensing wavelength range from 1 to 2.5  $\mu$ m for high SNR FT-NIR spectroscopy*. 2001.
31. Dries, J.C., et al., *Extended wavelength InGaAs detectors-recent progress in new materials for bandgap wavelengths  $\lambda$ >1.65  $\mu$ m*. 1999.

32. D'Hondt, M., et al., *Influence of buffer layer and processing on the dark current of 2.5  $\mu$ m-wavelength 2%-mismatched InGaAs photodetectors*. Optoelectronics, IEE Proceedings-, 1997. **144**(5): p. 277-282.
33. Takasaki, H., et al., *Photoluminescence properties of In<sub>0.53</sub>Ga<sub>0.47</sub>As/GaAs<sub>0.5</sub>Sb<sub>0.5</sub> type II quantum well structures lattice-matched to InP*. Applied Surface Science, 2000. **159**: p. 528-531.
34. Yamamoto, A., et al., *Optical properties of GaAs<sub>0.5</sub>Sb<sub>0.5</sub> and In<sub>0.53</sub>Ga<sub>0.47</sub>As/GaAs<sub>0.5</sub>Sb<sub>0.5</sub> type II single hetero-structures lattice-matched to InP substrates grown by molecular beam epitaxy*. Journal of crystal growth, 1999. **201**: p. 872-876.
35. Peter, M., et al., *Light-emitting diodes and laser diodes based on a Ga[<sub>sub</sub> 1 - x]In[<sub>sub</sub> x]As/GaAs[<sub>sub</sub> 1 - y]Sb[<sub>sub</sub> y] type II superlattice on InP substrate*. Applied Physics Letters, 1999. **74**(14): p. 1951-1953.
36. Cho, A., *A review of molecular beam epitaxy for optoelectronic applications*. Quantum Electronics, IEEE Journal of, 1975. **11**(9): p. 881-882.
37. Cho, A.Y. and J.R. Arthur, *Molecular Beam Epitaxy*. Progress in Solid-State Chemistry, 1975. **10**(Part 3): p. 157-191.
38. Parker, E.H.C., *The Technology and physics of molecular beam epitaxy*. 1985: New York : Plenum Press.
39. Herman, M.A. and H. Sitter, *Molecular beam epitaxy : fundamentals and current status*. 2nd, rev. and updated ed. ed. 1997: Berlin ; New York : Springer.
40. Xiaoguang, S., *High Performance 1300 nm Photodetectors Grown by Molecular Beam Epitaxy*. Electrical and Computer Engineering Department, University of Texas at Austin 2002. **Ph. D.**
41. Lenox, C.V., *High-Speed Resonant-Cavity-Enhanced Avalanche Photodiodes for Fiber Optic Applications*. Electrical and Computer Engineering Department, The University of Texas at Austin 1998. **Ph.D.**
42. B.D. Cullity, S.R.S., *Elements of x-ray diffraction*. 3rd ed. ed. 2001, Upper Saddle River, NJ: Prentice Hall.
43. Kelly, D., *Determination of lattice parameters in partially-relaxed thin epitaxial layers*. 2005.
44. Yamada, M., et al., *Low-threshold operation of 1.3- $\mu$ m GaAsSb quantum-well lasers directly grown on GaAs substrates*. Photonics Technology Letters, IEEE, 2000. **12**(7): p. 774-776.
45. Nakagawa, S., et al., *1.55- $\mu$ m InP-lattice-matched VCSELs with AlGaAsSb-AlAsSb DBRs*. Selected Topics in Quantum Electronics, IEEE Journal of, 2001. **7**(2): p. 224-230.

46. Lenox, C., *High-Speed Resonant-Cavity-Enhanced Avalanche Photodiodes for Fiber Optic Applications*. Electrical Engineering, The University of Texas at Austin 1998: p. 121.
47. Forrest, S., *Performance of  $In_xGa_{1-x}As_yP_{1-y}$  photodiodes with dark current limited by diffusion, generation recombination, and tunneling*. Quantum Electronics, IEEE Journal of, 1981. **17**(2): p. 217-226.
48. McIntyre, R.J., *Multiplication noise in uniform avalanche diodes*. Electron Devices, IEEE Transactions on, 1966. **13**(1): p. 164-168.
49. Anselm, K.A., et al., *Performance of thin separate absorption, charge, and multiplication avalanche photodiodes*. IEEE J. Quantum Electron, 1998. **34**: p. 482-490.
50. Yang, Q.K., et al., *Investigation of trap-assisted tunneling current in  $InAs/(GaIn)Sb$  superlattice long-wavelength photodiodes*. Applied Physics Letters, 2002. **81**(25): p. 4757-4759.
51. McIntyre, R., *Multiplication Noise in Uniform Avalanche Diodes*. IEEE Transactions Electron Devices, 1966. **ED-13**(1): p. 164.
52. Anselm, K.A., et al., *Characteristics of GaAs and AlGaAs Homojunction Avalanche Photodiodes with Thin Multiplication Regions*.
53. Zheng, X.G., et al., *Temperature dependence of the ionization coefficients of  $Al_xGa_{1-x}As$* . Quantum Electronics, IEEE Journal of, 2000. **36**(10): p. 1168-1173.
54. Shuling, W., et al., *Ultra-low noise avalanche photodiodes with a "centered-well" multiplication region*. Quantum Electronics, IEEE Journal of, 2003. **39**(2): p. 375-378.
55. Wang, S., et al. *Low-noise InP-based avalanche photodiodes with an impact-ionization-engineered multiplication region*. 2002.
56. Wang, S., et al., *Low-noise avalanche photodiodes with graded impact-ionization-engineered multiplication region*. Photonics Technology Letters, IEEE, 2001. **13**(12): p. 1346-1348.
57. Van de Walle, C.G., *Band lineups and deformation potentials in the model-solid theory*. Physical Review B, 1989. **39**(3): p. 1871-1883.
58. Itzler, M.A., et al., *Manufacturable planar bulk-InP avalanche photodiodes for 10 Gb/s applications*. 1999.
59. Itzler, M.A., et al., *High-performance, manufacturable avalanche photodiodes for 10 Gb/s optical receivers*. 2000.
60. Itzler, M.A., et al. *Planar bulk InP avalanche photodiode design for 2.5 and 10 Gb/s applications*. 1998.
61. Campbell, J.C., et al., *Frequency response of InP/InGaAsP/InGaAs avalanche photodiodes*. Journal of Lightwave technology, 1989. **7**(5): p. 778-784.

62. Wang, S., et al., *Low-noise impact-ionization-engineered avalanche photodiodes grown on InP substrates*. Photonics Technology Letters, IEEE, 2002. **14**(12): p. 1722-1724.
63. Anselm, K.A., et al., *Resonant Cavity-enhanced avalanche photodiodes grown by molecular beam epitaxy on InP for detection near 1.55  $\mu\text{m}$* . Journal of Vacuum Science and Technology B, 1998. **16**(3): p. 1426-1429.
64. Kinsey, G.S., et al., *Waveguide  $\text{In}_{0.53}\text{Ga}_{0.47}\text{As-In}_{0.52}\text{Al}_{0.48}\text{As}$  avalanche photodiode*. Photonics Technology Letters, IEEE, 2000. **12**(4): p. 416-418.

## Publications

### JOURNAL PAPERS:

- "A 2.4 $\mu\text{m}$  cutoff wavelength avalanche photodiode on InP substrate," R. Sidhu, L. Zhang, N. Tan, N. Duan, J. C. Campbell, A. L. Holmes, Jr., J. Hsu, M. Itzler, Submitted to Electronics Letters
- "A long-wavelength photodiode on InP using lattice-matched GaInAs-GaAsSb type-II quantum wells," R. Sidhu, N. Duan, J. C. Campbell, A. L. Holmes, Jr., IEEE Photonics Technology Letters, 17 (12), December 2005, pp 2715-2717
- "GaAsSb resonant-cavity enhanced avalanche photodiode operating at 1.06 $\mu\text{m}$ ," R. Sidhu, H. Chen, N. Duan, G. V. Karve, J. C. Campbell, and A. L. Holmes, Jr., Electronics Letters, 40 (20), September 2004, pp 1296-1297
- "Inert gas maintenance for molecular-beam epitaxy," M. M. Oye, J. Ahn, C. Cao, H. Chen, W. Fordyce, D. Gazula, S. Govindaraju, J. B. Hurst, S. Lipson, D. Lu, J. M. Reifsnider, O. Shehekin, R. Sidhu, X. Sun, D. G. Deppe, A. L. Holmes, Jr., and Terry J. Mattord, Journal of Vacuum Science and Technology B, 23, 2005, pp 1257
- "Diffusion mechanisms of indium and nitrogen during the annealing of InGaAs quantum wells with GaNAs barriers and GaAs spacer layers," M. M. Oye, S. Govindaraju, R. Sidhu, J. M. Reifsnider, and A. L. Holmes, Jr., Applied Physics Letters, 86, April 2005
- "High-saturation-current InGaAs/InAlAs charge-compensated uni-traveling-carrier photodiode," N. Li, R. Sidhu, X. Li, F. Ma, S. Demiguel, X. Zhen, A. L. Holmes Jr., J. C. Campbell, D. A. Tulchinsky, K. J. Williams; Physica Status Solidi A, 201 (13), October 2004, pp 3037-3041
- "InGaAs/InAlAs Avalanche Photodiode with Undepleted Absorber," N. Li, R. Sidhu, X. Li, F. Ma, X. Zheng, S. Wang, G. Karve, S. Demiguel, A. L. Holmes, Jr., and J. C. Campbell, Applied Physics Letters, 82 (13), March 2003, pp 2175-2177
- "Ultra-low noise avalanche photodiodes with "centered-well" multiplication region," S. Wang, F. Ma, X. Li, R. Sidhu, X. Zheng, X. Sun, A. L.

Holmes, Jr., and J. C. Campbell, IEEE Journal of Quantum Electronics, 39 (2), February 2003, pp 375 -378

"A Study of Low-Bias Photocurrent Gradient of Avalanche Photodiodes," S. Wang, R. Sidhu, G. Karve, F. Ma, X. Li, X. Zheng, J. B. Hurst, X. Sun, N. Li, A. L. Holmes, Jr., and J. C. Campbell, Transactions on Electron Devices, 49 (12), December 2002, pp 2107 – 2113

"Low-noise impact-ionization-engineered avalanche photodiodes grown on InP substrates," S. Wang, J. B. Hurst, F. Ma, R. Sidhu, X. Sun, X. G. Zheng, A. L. Holmes, Jr., A. Huntington, L. A. Coldren, J. C. Campbell, IEEE Photonics Technology Letters , 14 (12) , December 2002, pp 1722 -1724

"Improved optical coupling in waveguide photodetectors incorporating a wedge-shaped input facet," G. S. Kinsey, R. Sidhu, A. L. Holmes, Jr., and J. C. Campbell, Optics Letters, 27 (9), May 2002, pp 749-750

"GaAsSb: a novel material for near infrared photodetectors on GaAs substrates," X. Sun, S. Wang, J. Hsu, R. Sidhu, X.G. Zheng, X. Li, J. C. Campbell, and A. L. Holmes, Jr., IEEE Journal of Selected Topics in Quantum Electron, 8 (4), 2002, pp 817-822

"Low-noise avalanche photodiodes with graded impact-ionization-engineered multiplication region," S. Wang, R. Sidhu, X. G. Zheng, X. Li, X. Sun, A. L. Homes, Jr., and J. C. Campbell, IEEE Photonics Technology Letters, 13(12), December 2001, pp 1346-1348

#### **CONFERENCE PRESENTATIONS:**

"A 2.4 $\mu$ m cutoff wavelength avalanche photodiode on Indium Phosphide," R. Sidhu, L. Zhang, N. Tan, N. Duan, J. C. Campbell, A. L. Holmes, Jr., J. Hsu, M. Itzler, Late news papers, IEEE/LEOS Annual Meeting, 2005

"InP based photodiodes operating beyond 2 $\mu$ m using lattice-matched GaInAs-GaAsSb type-II quantum wells," R. Sidhu, N. Duan, J. C. Campbell, A. L. Holmes, Jr., Electronics Materials Conference (EMC), 2005

"A 2.3 $\mu$ m cutoff wavelength photodiode on InP using lattice-matched GaInAs-GaAsSb type-II quantum wells," R. Sidhu, N. Duan, J. C. Campbell, A. L.



- Holmes, Jr., Indium Phosphide and Related Materials Conference (IPRM), 2005
- “GaAsSb resonant-cavity enhanced avalanche photodiode operating at 1.06 $\mu$ m,” R. Sidhu, H. Chen, N. Duan, G. V. Karve, J. C. Campbell, A. L. Holmes, Jr., IEEE/LEOS Annual Meeting, 2004
- “Influence of growth parameters on Antimony incorporation during Molecular Beam Epitaxy of III-Arsenide-Antimonides,” R. Sidhu, X. Sun, and A. L. Holmes, Jr., Electronic Materials Conference, 2002
- “Ultralow-noise avalanche photodiodes,” J. C. Campbell, S. Wang, X. G. Zheng, G. S. Kinsey, A. L. Holmes, Jr., X. Sun, R. Sidhu, and P. Yuan, Proc. SPIE, Volume 4283, pp 480-488, Physics and Simulation of Optoelectronic Devices IX, 2001
- “High-speed waveguide avalanche photodetectors,” G. S. Kinsey, R. Sidhu, A. L. Holmes, Jr., and J. C. Campbell, Device Research Conference (DRC), 2001, pp 149-150
- “MEE-Grown InGaAs Quantum Dots Embedded in an In<sub>x</sub>Ga<sub>1-x</sub>As ( $x < 0.2$ ) Matrix for 1.3  $\mu$ m Emission,” S. Govindaraju, R. Sidhu, and A. L. Holmes, Jr., MRS Proceedings, 2000
- “MBE Growth and Device Performance of GaAsSb Resonant-Cavity-Enhanced Avalanche Photodiodes with Separate Absorption, Charge and Multiplication Regions,” X. Sun, S. Wang, R. Sidhu, X. G. Zheng, X. Li, J. C. Campbell, and A. L. Holmes, Jr., Electronic Materials Conference, 2002
- “Low noise avalanche photodiodes with a graded Impact-Ionization-Engineered multiplication region,” S. Wang, R. Sidhu, X.G. Zheng, X. Sun, A.L. Holmes, Jr., and J. C. Campbell, Device Research Conference, Late news, 2002
- “Low-noise InP-based avalanche photodiodes with an Impact-Ionization-Engineered multiplication region,” S. Wang, J. B. Hurst, F. Ma, R. Sidhu, X. Sun, X. G. Zheng, A. L. Holmes, Jr., J. C. Campbell, A. Huntington, and L. A. Coldren, IEEE/LEOS Annual Meeting, 2002, pp 488-489
- “Recent developments in avalanche photodiodes,” J. C. Campbell, S. Wang, X. Zheng, X. Li, N. Li, F. Ma, X. Sun, J. B. Hurst, R. Sidhu, A. L. Holmes,

Jr., A. Huntington, L. A. Coldren, Conference on Optoelectronic and Microelectronic Materials and Devices, 2002 , pp 53 – 58

## VITA

Rubin Sidhu was born in Ludhiana, India, on September 24, 1975, the eldest son of Rajinderpal Kaur Sidhu and Harminder Singh Sidhu. He earned the Indian School Certificate from Yadavindra Public School, Patiala, in 1994. In 1995, he entered the Regional Engineering College, Trichy, where he earned the Bachelor of Engineering degree in 1999. From 1999 to 2005, he attended the Graduate School at the University of Texas at Austin.

Permanent address: c/o S. Satpal Singh Toor  
Sawaddi Kalan  
Distt. Ludhiana, PB 142025  
India

This dissertation was typed by the author.